The Astrophysical Journal, 902:109 (29pp), 2020 October 20 https://doi.org/10.3847/1538-4357/abb82f

The ALMA Spectroscopic Survey in the Hubble Ultra Deep Field: CO Excitation and Atomic Carbon in Star-forming Galaxies at $z = 1$–3

Leindert A. Boogaard[1], Paul van der Werf[1], Axel Weiss[2], Gergö Popping[3], Roberto Decarli[4], Fabian Walter[5,6], Manuel Aravena[7], Rychard Bouwens[1], Dominik Riechers[5,8], Jorge González-López[7,9], Ian Smail[10], Chris Carilli[6,11], Melanie Kaasinen[5,12], Emanuele Daddi[13], Pierre Cox[14], Tanio Díaz-Santos[7,15,16], Hanae Inami[17], Paulo C. Cortes[18,19], and Jeff Wagg[20]

[1] Leiden Observatory, Leiden University, P.O. Box 9513, NL-2300 RA Leiden, The Netherlands; boogaard@strw.leidenuniv.nl
[2] Max-Planck-Institut für Radioastronomie, Auf dem Hügel 69, D-53121 Bonn, Germany
[3] European Southern Observatory, Karl-Schwarzschild-Str. 2, D-85748 Garching, Germany
[4] INAF-Osservatorio di Astrofisica e Scienza dello Spazio, via Gobetti 93/3, I-40129 Bologna, Italy
[5] Max Planck Institute für Astronomie, Königstuhl 17, D-69117 Heidelberg, Germany
[6] National Radio Astronomy Observatory, Pete V. Domenici Array Science Center, P.O. Box O, Socorro, NM 87801, USA
[7] Núcleo de Astronomía de la Facultad de Ingeniería y Ciencias, Universidad Diego Portales, Av. Ejército Libertador 441, Santiago, Chile
[8] Cornell University, 220 Space Sciences Building, Ithaca, NY 14853, USA
[9] Instituto de Astrofísica, Facultad de Física, Pontificia Universidad Católica de Chile Av. Vicuña Mackenna 4860, 782-0436 Macul, Santiago, Chile
[10] Centre for Extragalactic Astronomy, Department of Physics, Durham University, South Road, Durham, DH1 3LE, UK
[11] Battcock Centre for Experimental Astrophysics, Cavendish Laboratory, Cambridge CB3 0HE, UK
[12] Universität Heidelberg, Zentrum für Astronomie, Institut für Theoretische Astrophysik, Albert-Ueberle-Straße 2, D-69120 Heidelberg, Germany
[13] Laboratoire AIM, CEA/DSM-CNRS-Universite Paris Diderot, Irfu/Service d'Astrophysique, CEA Saclay, Orme des Merisiers, F-91191 Gif-sur-Yvette cedex, France
[14] Institut d'astrophysique de Paris, Sorbonne Université, CNRS, UMR 7095, 98 bis bd Arago, F-7014 Paris, France
[15] Chinese Academy of Sciences South America Center for Astronomy (CASSACA), National Astronomical Observatories, CAS, Beijing 100101, People's Republic of China
[16] Institute of Astrophysics, Foundation for Research and Technology—Hellas (FORTH), Heraklion, GR-70013, Greece
[17] Hiroshima Astrophysical Science Center, Hiroshima University, 1-3-1 Kagamiyama, Higashi-Hiroshima, Hiroshima 739-8526, Japan
[18] Joint ALMA Observatory—ESO, Av. Alonso de Córdova, 3104, Santiago, Chile
[19] National Radio Astronomy Observatory, 520 Edgemont Road, Charlottesville, VA 22903, USA
[20] SKA Organization, Lower Withington, Macclesfield, Cheshire SK11 9DL, UK
Received 2020 May 18; revised 2020 August 26; accepted 2020 August 31; published 2020 October 19

Abstract

We investigate the CO excitation and interstellar medium (ISM) conditions in a cold gas mass-selected sample of 22 star-forming galaxies at $z = 0.46$–3.60, observed as part of the ALMA Spectroscopic Survey in the Hubble Ultra Deep Field (ASPECS). Combined with Very Large Array follow-up observations, we detect a total of 34 CO $J \rightarrow J-1$ transitions with $J = 1$ up to 8 (and an additional 21 upper limits, up to $J = 10$) and 6 [C I] $^3P_1 \rightarrow {}^3P_0$ and $^3P_2 \rightarrow {}^3P_1$ transitions (and 12 upper limits). The CO(2–1) and CO(3–2)-selected galaxies, at $\langle z \rangle = 1.2$ and 2.5, respectively, exhibit a range in excitation in their mid-$J = 4$, 5 and high-$J = 7$, 8 lines, on average lower than ($L_{\rm IR}$-brighter) *BzK*-color- and submillimeter-selected galaxies at similar redshifts. The former implies that a warm ISM component is not necessarily prevalent in gas mass-selected galaxies at $\langle z \rangle = 1.2$. We use stacking and Large Velocity Gradient models to measure and predict the average CO ladders at $z < 2$ and $z \geqslant 2$, finding $r_{21} = 0.75 \pm 0.11$ and $r_{31} = 0.77 \pm 0.14$, respectively. From the models, we infer that the galaxies at $z \geqslant 2$ have intrinsically higher excitation than those at $z < 2$. This fits a picture in which the global excitation is driven by an increase in the star formation rate surface density of galaxies with redshift. We derive a neutral atomic carbon abundance of $(1.9 \pm 0.4) \times 10^{-5}$, comparable to the Milky Way and main-sequence galaxies at similar redshifts, and fairly high densities ($\geqslant 10^4$ cm^{-3}), consistent with the low-J CO excitation. Our results imply a decrease in the cosmic molecular gas mass density at $z \geqslant 2$ compared to previous ASPECS measurements.

Unified Astronomy Thesaurus concepts: CO line emission (262); Dust continuum emission (412); Interstellar medium (847); Galaxy formation (595); Galaxy evolution (594); High-redshift galaxies (734); Millimeter astronomy (1061)

1. Introduction

Cold molecular gas is the fuel for star formation. Characterizing the mass of the cold interstellar medium (ISM) and the internal physical conditions (temperature, density, and radiation field) is therefore fundamental to our understanding of the process of star formation (see the reviews by McKee & Ostriker 2007; Kennicutt & Evans 2012; and Carilli & Walter 2013). The majority of the star formation at intermediate redshifts ($z = 1$–3) takes place in galaxies that have an average star formation rate (SFR) for their stellar mass. These galaxies lie on the 'main sequence of star-forming galaxies (SFGs)'—the empirical correlation between the stellar mass and SFR of galaxies across cosmic time (e.g., Noeske et al. 2007; Elbaz et al. 2011; Whitaker et al. 2014; Schreiber et al. 2015; Boogaard et al. 2018). Although measurements of the molecular gas mass in these galaxies are now more frequently conducted, the physical conditions in the cold ISM of SFGs at $z > 1$ are still poorly constrained.

The mass of the molecular ISM is dominated by H_2, which does not radiate under typical conditions, and must therefore be traced by other species. The most common and direct tracer of the molecular gas mass is the first rotational transition of

carbon monoxide $^{12}C^{16}O$ $J = 1 \rightarrow 0$, hereafter CO(1–0) (e.g., Dickman et al. 1986; Solomon et al. 1987; Bolatto et al. 2008). Alternative tracers of the molecular gas mass include the dust emission (e.g., Hildebrand 1983; Magdis et al. 2012; Scoville et al. 2014, 2016; Magnelli et al. 2020) and lines from fainter optically thin species, such as neutral atomic carbon ([C I]; Papadopoulos et al. 2004; Weiß et al. 2005; Walter et al. 2011), now more frequently observed in SFGs at $z > 1$ (e.g., Popping et al. 2017; Valentino et al. 2018; Bourne et al. 2019).

Measurements of the molecular gas mass via CO at $z > 1$ are limited to the specific transitions that can be observed through the atmospheric windows from Earth. Constraints on the CO excitation are therefore crucial to convert observations from higher-J lines back to CO(1–0). The higher rotational levels of CO (with quantum number $J > 1$) are populated both radiatively and collisionally and the rotational ladder of CO is therefore a key probe of the density, n_{H_2}, and kinetic temperature, T_{kin}, of the emitting medium. The excitation of CO can be driven by a number of processes, related to star formation, (galactic) dynamics (including shocks/mechanical heating) and potential activity from an active galactic nucleus (AGN). In the local universe, observations with the Herschel satellite have shown that the CO excitation in (ultra)luminous infrared galaxies ((U)LIRGS) with $L_{IR} \geqslant 10^{11}$ (10^{12}) (Sanders & Mirabel 1996), can often be well modeled by the combination of a cold component (containing most of the mass) and a warm component, dominating the emission below and above $J \approx 4$ respectively, while heating from an AGN is the dominant contributor to the line emission only for the levels above $J \approx 10$ (e.g., van der Werf et al. 2010; Greve et al. 2014; Kamenetzky et al. 2014, 2017; Rosenberg et al. 2015; Lu et al. 2017). The CO excitation in sources at higher redshift has been a field of intense study, yet, to date, only limited constraints exist regarding the CO ladder in SFGs at $z > 1$.

At the time of the review by Carilli & Walter (2013), the main sources studied in multiple CO transitions at $z > 1$ were quasars (QSOs), radio galaxies, and submillimeter-selected galaxies (SMGs), with high $L_{IR} \gg 10^{12}$ $L_{\odot}$. Overall, these early results were indicative of decreasing excitation (i.e., a lower n_{H_2} and T_{kin}) going from quasars to SMGs. Since then, the average CO excitation of SMGs has been studied by Bothwell et al. (2013), who characterized a sample of mostly unlensed SMGs at $z = 2$–4, up to CO(7–6) (including CO(1–0) observations from Carilli et al. 2010; Riechers et al. 2010, 2011b; Ivison et al. 2011). Spilker et al. (2014) used Atacama Large Millimeter/submillimeter Array (ALMA) spectral scan observations of 22 lensed SMGs detected with the South Pole Telescope (SPT) at $z = 2$–6 (Weiß et al. 2013) to stack CO(3–2) up to CO(6–5). More recently, Yang et al. (2017) studied Herschel-selected, strongly lensed SMGs at $z = 2$–4 up to CO(8–7). These studies find that the CO ladders of SMGs can continue to rise up to $J \sim 7$, testifying to a warm and dense ($n \geqslant 10^{5.5}$ cm^{-3}) ISM. The differences between the (low-J) CO excitation in SMGs and (mid-IR selected) AGNs have not been found to be statistically significant (Sharon et al. 2016; Kirkpatrick et al. 2019).

In contrast, observations of CO excitation in main-sequence SFGs at $z > 1$ have only recently become possible, with the advent of the Northern Extended Millimeter Array and the ALMA. The Plateau de Bure Interferometer HIgh-z Blue Sequence Survey has observed CO(3–2) in a sample of massive, main-sequence-selected galaxies between $z = 1$–3 (Genzel et al. 2010, 2015; Tacconi et al. 2010, 2013, 2018), with multiline CO excitation follow-up of only a few sources (Bolatto et al. 2015; Brisbin et al. 2019). A number of SFGs, selected by their BzK-color (Daddi et al. 2004) and having a detection at 24 μm and 1.4 GHz (Daddi et al. 2010), have been observed in more than one CO transition from CO(1–0) to CO(3–2) (Dannerbauer et al. 2009; Daddi et al. 2010; Aravena et al. 2010, 2014). The CO ladder of four of these "BzK-selected" galaxies at $z \approx 1.5$ was characterized comprehensively by Daddi et al. (2015). They found all sources were significantly excited in their CO(5–4) transition, compared to the lower-J transitions, indicating the presence of both a cold and a denser, possibly warmer gas component. Very recently, Valentino et al. (2020a) expanded these results with observations of a larger sample of similarly IR-bright SFGs at $z = 1.25$. However, all these samples were preselected based on their SFR, and are still among the most massive and IR luminous main-sequence galaxies at these redshifts, with only specific sources selected for multiline follow-up. Therefore, it remains unclear whether the excitation conditions found in these sources are representative of the general population of SFGs at these redshifts, in particular at lower masses and SFRs.

The ALMA Spectroscopic Survey in the Hubble Ultra Deep Field (ASPECS; Walter et al. 2016) provides a unique avenue to study the CO excitation, molecular gas content and physical conditions of the cold ISM of SFGs at high redshift. ASPECS is a flux-limited survey, designed to detect CO in galaxies without preselection. It thereby provides the most complete inventory of the cosmic molecular gas density, $\rho_{H_2}(z)$, to date (Decarli et al. 2016a, 2019, 2020). The galaxies detected in CO by ASPECS are found to lie on, above, and below the main sequence at $z = 1$–3, with near-solar metallicities (Aravena et al. 2019; Boogaard et al. 2019). The coverage of ASPECS (Band 3 and Band 6) provides simultaneous constraints on multiple lines from CO, [C I] for most sources, depending on the redshift (as well as any other species in the frequency range). Furthermore, the multiple tunings scanning through the entire ALMA frequency bands give a high continuum sensitivity, providing a deep (9.3 μJy beam^{-1}, Section 2.1), contiguous continuum map at 1.2 mm in the Hubble Ultra Deep Field (HUDF; Aravena et al. 2020; González-López et al. 2020). Using earlier data from the ASPECS-Pilot program on a smaller area of the sky, Decarli et al. (2016b) studied a sample of seven galaxies at $z = 1$–3 (a subset of the sources studied in this paper), finding that the CO excitation conditions were overall lower than those typically found in starbursts, SMGs, and QSO environments.

This paper studies the CO excitation, atomic carbon emission and ISM conditions in a flux-limited sample of 22 CO and/or dust-continuum detected galaxies at $z = 1$–3 from the ASPECS Large Program (LP), supplemented by follow-up CO(1–0) observations from VLASPECS (Riechers et al. 2020). The paper is organized as follows. We first present the ALMA and Very Large Array (VLA) observations and the physical properties of the galaxies in the sample (Section 2). All line fluxes are measured homogeneously through simultaneous Gaussian fitting (Section 3) and presented in Section 4. We discuss the mid- and high-J CO excitation in the individual CO(2–1)- and CO(3–2)-selected sources at $\langle z \rangle = 1.2$ and $\langle z \rangle = 2.5$, respectively, in Section 5.1 and compute the average CO ladders through stacking (including individually undetected lines; Section 5.2). We then use Large Velocity Gradient

Table 1
Physical Properties of the ASPECS-LP Sample Considered in This Paper

ID 1mm	ID 3mm	ID 9mm	z	$\log M_*$ ($M_\odot$)	log SFR ($M_\odot$ yr^{-1})	$\log L_{\rm IR}$ ($L_\odot$)	$\log \Sigma_{\rm SFR}$ ($M_\odot$ yr^{-1} kpc^{-2})	r_e (arcsec)	X-ray
(1)	(2)	(3)	(4)	(5)	(6)	(7)	(8)	(9)	(10)
1mm.C01	3mm.01	9mm.1	2.543	10.4 ± 0.1	2.37 ± 0.10	12.9 ± 0.1	1.07 ± 0.19	0.21 ± 0.04	AGN
1mm.C03	3mm.04	⋯	1.414	11.3 ± 0.1	1.72 ± 0.13	12.0 ± 0.1	-0.82 ± 0.14	0.88 ± 0.04	⋯
1mm.C04	3mm.03	9mm.6	2.454	10.7 ± 0.2	1.78 ± 0.21	11.9 ± 0.2	-0.46 ± 0.22	0.63 ± 0.04	⋯
1mm.C05	3mm.05	⋯	1.551	11.5 ± 0.1	1.79 ± 0.17	12.0 ± 0.2	-0.83 ± 0.18	0.98 ± 0.04	AGN
1mm.C06	3mm.07	9mm.3	2.696	11.1 ± 0.1	2.32 ± 0.14	12.4 ± 0.1	0.10 ± 0.15	0.61 ± 0.04	⋯
1mm.C07	⋯	9mm.7	2.580	11.0 ± 0.1	1.65 ± 0.14	11.9 ± 0.1	0.48 ± 0.24	0.18 ± 0.04	AGN
1mm.C09	3mm.13	⋯	3.601	9.8 ± 0.2	1.58 ± 0.21	11.6 ± 0.2	0.06 ± 0.25	0.27 ± 0.04	⋯
1mm.C10	⋯	⋯	1.997	11.1 ± 0.1	2.04 ± 0.10	12.4 ± 0.1	-0.16 ± 0.12	0.60 ± 0.04	X
1mm.C12	3mm.15	⋯	1.096	9.5 ± 0.1	1.55 ± 0.10	11.7 ± 0.1	-0.82 ± 0.11	0.73 ± 0.04	AGN
1mm.C13	3mm.10	⋯	1.037	11.1 ± 0.1	1.27 ± 0.10	11.6 ± 0.1	-0.36 ± 0.15	0.31 ± 0.04	⋯
1mm.C14a	⋯	9mm.5	1.999	10.8 ± 0.1	1.70 ± 0.17	11.9 ± 0.2	0.20 ± 0.22	0.27 ± 0.04	⋯
1mm.C16	3mm.06	⋯	1.095	10.6 ± 0.1	1.52 ± 0.10	11.5 ± 0.1	-0.76 ± 0.11	0.66 ± 0.04	X
1mm.C15	3mm.02	⋯	1.317	11.2 ± 0.1	1.05 ± 0.12	11.5 ± 0.1	-0.95 ± 0.14	0.48 ± 0.04	⋯
1mm.C19	3mm.12	9mm.4	2.574	10.6 ± 0.1	1.54 ± 0.20	11.6 ± 0.2	-0.43 ± 0.21	0.46 ± 0.04	AGN
1mm.C20	⋯	⋯	1.093	10.9 ± 0.1	0.97 ± 0.14	11.2 ± 0.1	-1.01 ± 0.16	0.46 ± 0.04	⋯
1mm.C25	3mm.14	⋯	1.098	10.6 ± 0.1	1.35 ± 0.11	11.4 ± 0.1	-0.00 ± 0.19	0.22 ± 0.04	⋯
1mm.C23	3mm.08	⋯	1.382	10.7 ± 0.1	1.60 ± 0.12	11.7 ± 0.1	-1.03 ± 0.12	0.99 ± 0.04	⋯
1mm.C30	⋯	⋯	0.458	10.0 ± 0.1	1.12 ± 0.10	11.0 ± 0.1	-0.01 ± 0.22	0.17 ± 0.04	X
⋯	3mm.11	⋯	1.096	10.2 ± 0.1	0.99 ± 0.11	11.0 ± 0.1	-0.70 ± 0.15	0.33 ± 0.04	⋯
…[a]	3mm.09	9mm.2	2.698	11.1 ± 0.1	2.54 ± 0.10	12.6 ± 0.1	2.05 ± 0.42	0.08 ± 0.04	AGN
Faint.1mm.C20	3mm.16	⋯	1.294	10.3 ± 0.1	1.06 ± 0.14	11.0 ± 0.2	-1.10 ± 0.15	0.57 ± 0.04	⋯
⋯	MP.3mm.2	⋯	1.087	10.4 ± 0.1	1.40 ± 0.10	11.5 ± 0.1	-0.95 ± 0.11	0.71 ± 0.04	X

Notes. (1) ASPECS-LP continuum ID (Aravena et al. 2020; González-López et al. 2020). (2) ASPECS-LP line ID (Boogaard et al. 2019). (3) VLASPECS ID (Riechers et al. 2020) (4) Spectroscopic redshift. (5) Stellar mass. (6) SFR. (7) $L_{\rm IR}$(3–1000 μm). (8) SFR surface density $\Sigma_{\rm SFR} = {\rm SFR}/2\pi\ r_e^2$. (9) HST/F160W effective radius from van der Wel et al. (2012), for which we adopt an 0.″04 error floor. (10) X-ray classification as either hosting an AGN or another source of X-ray emission (X) (Luo et al. 2017). Columns (5)–(7) were derived with MAGPHYS (Da Cunha et al. 2008, 2015). We conservatively fold in a 0.1 dex error to the MAGPHYS uncertainties, to account for underestimated and systematic uncertainties, and report the values as $p_{50} \pm \sqrt{(0.5(p_{84} - p_{16}))^2 + 0.1^2}$, where p_i is the ith percentile.
[a] Object falls outside of the Band 6 mosaic, but is the brightest 1 mm continuum source in the ASPECS field (see Dunlop et al. 2017).

(LVG) models to characterize the average ladders at $z \leqslant 2$ and $z > 2$ (Section 5.3). We further analyze the low-J CO excitation by placing our galaxies on empirical relations with the rest-frame 850 μm dust luminosity (Section 5.4). We next turn to the neutral atomic carbon, discuss its mass and abundance, and use photodissociation regions (PDR) models to analyze the average ISM conditions in our galaxies (Section 6). The implications of our measurements on the average low-, mid-, and high-J CO excitation in SFGs at $z \geqslant 1$ are discussed in Section 7. Finally, we conclude with the implications of our results for the inference of the cosmic molecular gas density from ASPECS, as these are the galaxies that directly inform that measurement (Section 7.5). Throughout this paper, we use a Chabrier (2003) initial mass function and a concordance flat ΛCDM cosmology with $H_0 = 70\,{\rm km\,s^{-1}\,Mpc^{-1}}$, $\Omega_m = 0.3$, and $\Omega_\Lambda = 0.7$, in good agreement with the results from Planck Collaboration et al. (2016).

2. Observations and Ancillary Data

2.1. ALMA Spectroscopic Survey Data Reduction

The ASPECS data consists of two spectral scan mosaics over the deepest part of the HUDF (Illingworth et al. 2013; Koekemoer et al. 2013). The raw ASPECS data were processed with CASA (McMullin et al. 2007) as described in González-López et al. (2019) for Band 3 and Decarli et al. (2020) for Band 6. The visibilities were imaged using the task TCLEAN, adopting natural weighting. The complete mosaics cover an area of 4.6 arcmin^2 (Band 3) and 2.9 arcmin^2 (Band 6), measured as the region in which the primary beam (PB) sensitivity is ⩾50% of the peak sensitivity (6.1 and 3.7 arcmin^2 when measured down to 20%).

The Band 3 data cube ranges from 84 to 115 GHz, with a channel width of 7.813 MHz, corresponding to velocity resolution of $\Delta v \approx 23.5\,{\rm km\,s^{-1}}$ at 99.5 GHz. The spatial resolution of the naturally weighted cube is ≈1.″8 × 1.″5 (at 99.5 GHz). The sensitivity varies across the frequency range, reaching an average root-mean-square (rms) sensitivity per channel of ≈0.2 mJy beam^{-1}, varying across the frequency range (see González-López et al. 2019, Figure 3). The Band 6 data cube spans from 212–272 GHz, and was resampled at a channel width of 15.627 MHz, corresponding to $\Delta v \approx 19.4\,{\rm km\,s^{-1}}$ at 242 GHz. The naturally weighted cube has a beam size of ≈1.″5 × 1.″1 and reaches an average rms depth of ≈0.5 mJy beam^{-1} per channel (see Decarli et al. 2020, Figure 1).

To create continuum maps, we collapse both the Band 6 (1.2 mm) and Band 3 (3.0 mm) data cubes over their full frequency range. The deepest parts of the continuum reach 3.8 μJy beam^{-1} in Band 3, with a beam size of 2.″8 × 1.″7, and 9.3 μJy beam^{-1} in Band 6, with a beam size of 1.″5 × 1.″1 (González-López et al. 2019, 2020). The absolute flux calibration is expected to be reliable at the ∼10% level.

2.2. ASPECS Sample

We search for line and continuum sources in the ASPECS data cubes, which are described in González-López et al. (2019, 2020). In the Band 3 data we detect 16 CO emitters at high significance from the line search, plus 2 additional CO emitters based on a Multi Unit Spectroscopic Explorer (MUSE) redshift prior (Boogaard et al. 2019). For five of these sources we also detect the continuum at 3 mm (González-López et al. 2019). From the Band 6 data we detect 35 sources in 1.2 mm dust continuum at high significance, 32 of which show counterparts in the optical/near-IR imaging (Aravena et al. 2020; González-López et al. 2020). We conduct a search for emission lines in the Band 6 cube following the same approach as for the Band 3 data. This reveals several CO (and [C I]) emitters, all coinciding with sources detected in the Band 6 continuum image, with one exception: a narrow CO line in one of the CO emitters also found in Band 3 (3mm.11; not detected in continuum at all). Notably, we did not find any high-significance lines in sources not already detected in the dust continuum. The Band 6 continuum sources furthermore encompass all Band 3 CO emitters (Aravena et al. 2020), with four exceptions: the first two are the lowest mass and SFR source of the main sample (3mm.11) and the faintest source in CO (ASPECS-LP-MP.3mm.02). The third is 3mm.16, which does however have a dust-continuum counterpart in the supplementary catalog of 26 sources at lower significance (the "Faint" sample), which were selected based on the presence of a optical/near-IR counterpart (González-López et al. 2020). The fourth is 3mm.09, which is the brightest source at 1.3 mm in the field (UDF1; Dunlop et al. 2017). This source was detected toward the edge of the Band 3 mosaic (at 40% of the primary beam peak sensitivity, hereafter PB response) and is at the extreme edge of the Band 6 mosaic. The CO(7–6) and [C I](2–1) lines lie at 6% of the PB response at 218 GHz and the source falls outside the continuum map (below 10% PB response). We do include this source in this paper, but note that the upper limits on the lines in Band 6 are essentially unconstraining. For the SED fitting (Section 2.4) we use the continuum measurement at 1.3 mm.

We therefore consider all of the Band 3 and Band 6 continuum and line sources that are detected in at least one line. In total, the sample consists of 22 sources. The majority of the sample is low-J CO-selected in Band 3 (17/22). There are five exceptions, i.e., sources which are added based on the Band 6 data. Three sources lack coverage of any CO lines in Band 3. These include (1mm.C10 and C14a) at $z \approx 1.99$ and 1mm.C30 at $z = 0.46$. One source, 1mm.C20, does not show CO lines in Band 3 nor 6, but is detected in [C I] in Band 6. Lastly, we report a new CO(3–2) detection for 1mm.C07 in Band 3. This source was not included in the original sample from González-López et al. (2019) because the line is below their single-line fidelity threshold and the source lacks a MUSE redshift. However, this source is now confirmed through the detection of the high-J CO and [C I] lines in Band 6. One Band 3 CO(2–1) emitter (MP.3mm.1; based on a MUSE prior) is not included in this paper, because we re-measure the integrated flux to be slightly below 3σ. This is likely because we convolve both cubes to a slightly larger beam size, in order to consistently measure the line ratios, at the cost of signal-to-noise ratio (S/N; see Section 3.1).

The full sample is listed in Table 1. It spans redshifts from $z = 0.46$–3.60, with the majority of the sample being at $z = 1$–3. We show the redshift distribution in Figure 1, highlighting the spectral lines covered by ASPECS in the top panels. The final redshifts are determined from our fits of the CO and/or [CI] line(s), using the redshifts from the MUSE HUDF survey and our literature compilation (see Boogaard et al. 2019; Decarli et al. 2019) as prior information (Section 3.1).

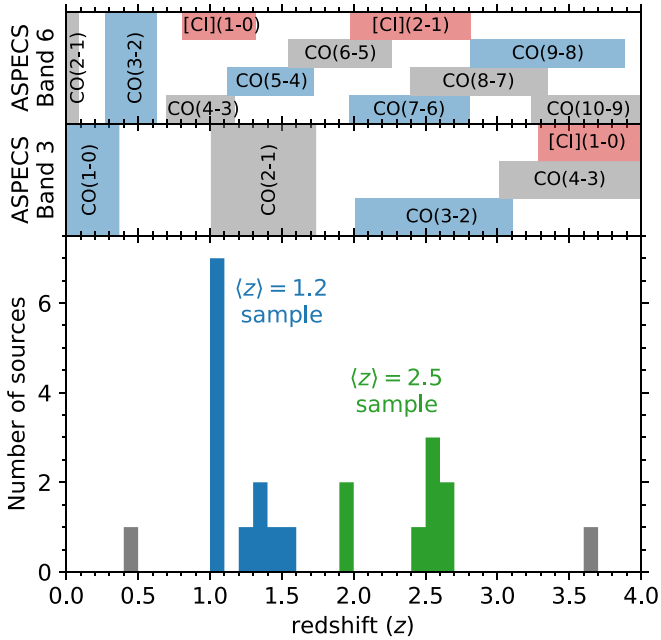

Figure 1. Redshift distribution of the ASPECS sources discussed in this paper (bottom panel). The top panels indicate the lines covered by ASPECS in Band 3 and Band 6 at different redshift ranges (colored just to make them more easily distinguishable). We highlight the samples at $z = 1.0$–1.6 (blue) and $z = 2.0$–2.7 (green), for which we have coverage of both a low-J and a mid/high-J CO line. Additional VLA CO(1−0) follow-up is available for all but one source in the $\langle z \rangle = 2.5$ sample (Section 2.3; Riechers et al. 2020).

2.3. Very Large Array Observations (VLASPECS)

The CO(1–0) transition in the ASPECS galaxies between $z = 1.99$–2.70 was observed with the Karl G. Jansky VLA as part of the VLASPECS survey (Riechers et al. 2020; VLA program ID: 19B-131; PI: Riechers). Two pointings were conducted with the D array in the *Ka* band, over a continuous bandwidth of 30.593–38.662 GHz at 2 MHz spectral resolution, resulting in a 17 km s^{-1} resolution (at 35 GHz). The naturally weighted cube has an average rms noise level of $\approx$0.1 mJy beam^{-1} channel^{-1} (increasing by about a factor of two from the low- to the high-frequency edge of the bandpass, as expected) and a beam size of $4\farcs99 \times 1\farcs96$. Given the recent flaring activity in the calibrator, the absolute flux is conservatively considered to be reliable at the $\sim$15% level. The full data reduction and presentation is part of Riechers et al. (2020). In this paper, we focus primarily on the CO excitation and analyze the data in concert with the higher-J CO lines.

2.4. Multiwavelength Data and SED Fitting

The wealth of multiwavelength photometry available over the HUDF provides good constraints on the spectral energy distribution (SED) of each of the ASPECS galaxies. By

modeling the SEDs using the MAGPHYS (Da Cunha et al. 2008, 2015), we derive stellar masses, SFRs and IR luminosities ($L_{\rm IR}$; 3–1000 μm). We follow the same procedure as described in Boogaard et al. (2019), utilizing the UV—24 μm photometry from the 3D-HST survey (Skelton et al. 2014; Whitaker et al. 2014), in combination with the Herschel 70–160 μm data from Elbaz et al. (2011) and the 3 mm continuum from González-López et al. (2019). Superseding the earlier fits, we now include the updated 1.2 mm flux measurements from González-López et al. (2020). Furthermore, we include 5σ upper limits of 50 μJy and 20 μJy in the case of a non-detection at 1.2 mm and 3 mm, respectively. The fits for the full dust-continuum sample (including the sources not detected in CO) are presented in Aravena et al. (2020). Following Aravena et al. (2020), we conservatively fold in an additional 0.1 dex to the error bars to account for underestimated and systematic uncertainties. We derive average SFR surface densities, $\Sigma_{\rm SFR} = {\rm SFR}/2\pi r_e^2$, using the HST/F160W half-light radii (r_e) from van der Wel et al. (2012). This is a reasonable approximation for sources in which the radial extent of the star formation follows the stellar disk, but should be considered as a lower limit in the case of a more nuclear starburst. The formal errors on the radii are an of order a few percent of the point-spread function (PSF $\sim 0\farcs16$), which we find to be very small. Hence, we conservatively adopt a floor on the error bar of PSF/4 $= 0\farcs04$. Lastly, the X-ray sources in the ASPECS sample are identified and classified using the deep Chandra 7 Ms data from Luo et al. (2017) as described in Boogaard et al. (2019).

3. Methods

3.1. Spectral Line Analysis

We extract single pixel spectra from the naturally weighted Band 3 and Band 6 cubes, convolved to a common beam size of $2\farcs2$. In this way, we ensure that the line fluxes are extracted over the same region of the galaxy, while minimizing the impact of flux loss for sources that are more slightly extended than the beam size of the naturally weighted cube. We use the cubes at their native spectral resolution in order to resolve even the narrowest lines ($\sim$50 km s^{-1}) into several resolution elements. We adopt the position of the dust-continuum detection (Aravena et al. 2020; González-López et al. 2020), or, in the case of no dust-continuum detection, the CO line positions (Boogaard et al. 2019; González-López et al. 2019). The beam size of the VLA data is already larger than that of ASPECS ($\approx 5\farcs0 \times 2\farcs0$) and only the brightest two sources are slightly resolved along the minor axis by the VLA (similar to what is seen in ASPECS, which motivated the convolution to $2\farcs2$). We therefore use the spectra extracted by Riechers et al. (2020) in order to measure the flux over as-similar regions as possible.

For each source, we simultaneously fit all CO and [CI] lines that are expected to fall in Band 3, Band 6, and the VLA *Ka* band, based on the redshift from the line search, using the nonlinear least square fitting code LMFIT[21] (Newville et al. 2019). We first subtract the continuum in Band 6, which is determined by fitting a first order polynomial to the median filtered spectrum. All the lines in the continuum-free spectrum are modeled by Gaussian line shapes, whose central frequencies are tied together by a single redshift.

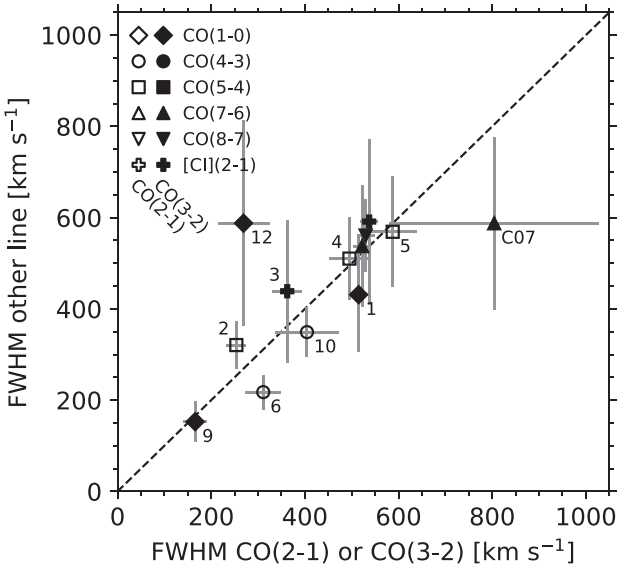

Figure 2. Comparison of the line width (full-width at half-maximum, FWHM) between the CO(2–1) and CO(3–2) lines (by which the sample was selected) and the higher-J CO ($J > 4$) or [C I] lines in individual ASPECS galaxies (extracted over the same $2\farcs2$ aperture), as well as CO(1–0) from the VLA. The sources were fit with a single redshift but allowing, *for this figure only*, a varying line width for each transition. Sources are identified by the 3mm.ID or else their 1mm.CID. We only show sources where the relevant lines are detected with a S/N > 3 in these fits. We add a small positive offset to the multiple lines of 3mm.1, for readability. Overall, we find consistent line widths between the low-J CO and higher-J CO/[C I] lines. Throughout the analysis presented in this work, we will therefore use a fixed line width to model the different transitions of a particular source, which is determined by fitting all the lines simultaneously (see Section 3.1).

Fitting the sources with the highest S/N spectra, we find that the widths of the different transitions are consistent in most cases. This is illustrated in Figure 2, where we show the line width measured in the CO(2–1) and CO(3–2) lines in Band 3 against the line width of the other CO and [C I] lines. Here we only include sources with S/N > 3 in all the relevant lines in the free fit (which is more conservative than for the fits where the line widths are tied together, because of the additional degrees of freedom). We therefore model all the lines with a single line width. Although this assumption is not strictly necessary, this often improves the fitting of lines with lower S/N, where the line width can be better constrained by the strongest lines. The integrated line fluxes are consistent within the uncertainties regardless of whether we force the widths of the lines to match. Furthermore, fitting the non-detected lines simultaneously does not influence the fit of the detected lines within the error (even in the most extreme case of a single detection and multiple upper limits). The observed line widths are likely governed by the global kinematics of the source. As such, the consistent line widths between the different transitions suggest that the gas is not much more compact or extended in some transitions compared to others, which supports our analysis of the global CO excitation (see Appendix A for further discussion).

As an illustration of the fitting procedure, we show the complete Band 3 and 6 spectrum of the brightest source, 1 mm. C01, in Figure 3, together with the best-fit model (lines and continuum). This particular source is detected in multiple lines as well as the dust continuum.

[21] https://lmfit.github.io/lmfit-py/

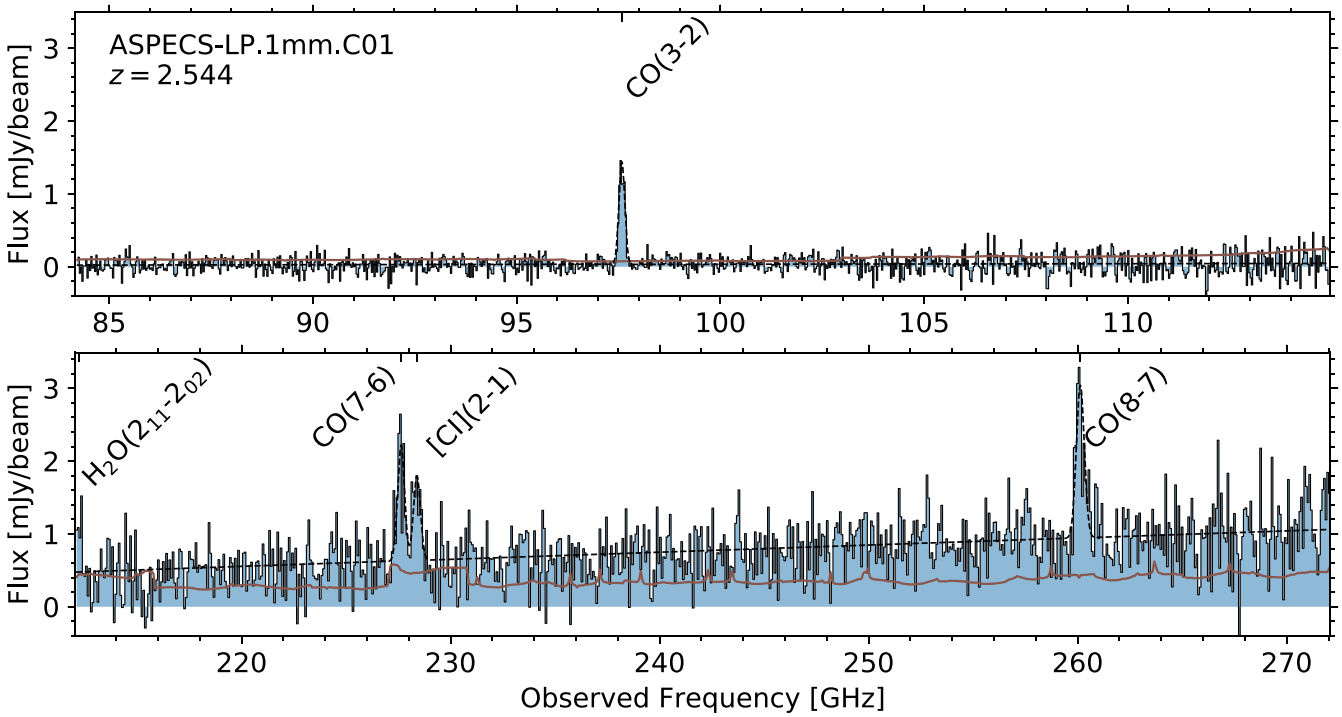

Figure 3. Full spectrum in Band 3 (Top) and Band 6 (Bottom) of ASPECS-LP.1mm.C01, shown as an example of the ASPECS frequency coverage. The brown line shows the rms noise in each of the channels. For visualization purposes, the spectra are averaged to a similar resolution of 95 km s^{-1}. The black dashed line shows the best-fit model, which includes Gaussian line fits to the ^{12}CO and atomic carbon ([C I]) lines (constrained in redshift and line width by all the lines simultaneously) and a linear continuum (Section 3.1). Note that in this particular source we also detect a water line at the edge of the Band 6, para $H_2O(2_{11} \rightarrow 2_{02})$, which is not included in the fitting (and not further discussed in the paper).

3.2. Deriving Line Luminosities and Molecular Gas Masses

The line luminosities are commonly expressed in different units, useful for different purposes, and we briefly review the relevant equations below (see Solomon & Vanden Bout 2005; Obreschkow et al. 2009; Carilli & Walter 2013). When expressed in solar luminosities, the line luminosities indicate the total power emitted,

$$L = 1.040 \times 10^{-3}\, S^V d_L^2 \nu_{\rm obs}\, L_\odot. \quad (1)$$

Units of integrated brightness temperature are convenient to derive the line excitation (notably, if the CO line emission originates in thermalized, optically thick regions, $L'_{\rm CO}$ is constant for all J levels),

$$L' = 3.255 \times 10^7\, S^V d_L^2 \nu_{\rm obs}^{-2} (1+z)^{-3}\ {\rm K\ km\ s^{-1}\ pc^2}. \quad (2)$$

In both equations, $S^V = \int S_\nu dv$ is the integrated line flux ($[S^V]$ = Jy km s^{-1}), d_L is the luminosity distance ($[d_L]$ = Mpc), and $\nu_{\rm obs}$ is the observed line frequency ($[\nu_{\rm obs}]$ = GHz) (Solomon et al. 1992). Note that the two definitions are proportional, with $L'_{\rm CO} = 3.130 \times 10^{-11} \nu_{\rm rest}^{-3} L_{\rm CO}$.

The CO excitation is typically reported as a brightness temperature ratio between two transitions, which is computed from $L'_{\rm CO}$ or S^V as

$$r_{J_2\,J_1} = \frac{L'_{{\rm CO}\,J_2\rightarrow J_2-1}}{L'_{{\rm CO}\,J_1\rightarrow J_1-1}} = \frac{S^V_{{\rm CO}\,J_2\rightarrow J_2-1}}{S^V_{{\rm CO}\,J_1\rightarrow J_1-1}} \left(\frac{J_1}{J_2}\right)^2. \quad (3)$$

The relationship between the molecular gas mass ($M_{\rm mol}$) and the CO luminosity ($L'_{\rm CO}$) is expressed as

$$M_{\rm mol} = \alpha_{\rm CO} \frac{L'_{{\rm CO}\,J\rightarrow J-1}}{r_{J1}}, \quad (4)$$

where $\alpha_{\rm CO}$ is the conversion factor between CO luminosity and the total molecular gas mass (including a factor of 1.36 to account for heavy elements, primarily Helium; see Bolatto et al. 2013 for a recent review). We adopt an $\alpha_{\rm CO} = 3.6\ M_\odot$ (K km s^{-1} pc^2)$^{-1}$ (Daddi et al. 2010) where needed (following the discussion in Boogaard et al. 2019 and consistent with the other ASPECS studies, as well as COLDz; Riechers et al. 2019).

4. Results

4.1. Observed Emission Lines from CO and [C I]

We detect emission lines from CO and/or [C I] in 22 distinct galaxies in the ASPECS field, between redshifts $z = 0.46$–3.60. For the CO $J \rightarrow J-1$ lines we measure 34 detections plus 21 upper limits, with rotational quantum numbers between $J = 1$ and 10. We only probe the frequency range for the CO(9–8) and CO(10–9) transitions in a single source at $z = 3.60$ but neither is detected. Therefore, we focus on the transitions up to CO(8–7). For atomic carbon we report six line detections plus 12 upper limits in the $^3P_1 \rightarrow {}^3P_0$ and $^3P_2 \rightarrow {}^3P_1$ transitions, hereafter [C I](1–0) and [C I](2–1).

We measure the integrated line fluxes as described in Section 3.1 and show the individual line fits for all sources in

Figure 15 in Appendix B. The resulting redshifts, line widths (FWHM), central frequencies, and line fluxes for all sources can be found in Table 6. In the remainder of this paper, we will treat tentative lines with an integrated line flux smaller than 3σ in the VLA and ALMA data as upper limits. Here, σ is the uncertainty on the Gaussian fit, measured over the same line width as the detected lines that they are tied to. As not all lines are perfectly described by single Gaussians, we also compute the line fluxes by integrating the channels within $1.4\times$ the FWHM and confirm these are consistent with the Gaussian fits to within error.

Our method forces all lines for a source to a common line width, which may result in different error bars for some lines than found based on an S/N optimized extraction of each individual line (González-López et al. 2019; Riechers et al. 2020). This more conservative treatment, which is chosen to minimize biases for the specific analysis carried out in this work, differs from the way they are used in other works in ASPECS focused on studies of the global gas density evolution (Decarli et al. 2019; Decarli et al. 2020; Riechers et al. 2020). Compared to the previous ASPECS papers, we find that our fluxes in Band 3 are on average 20% lower than those from González-López et al. (2019), but consistent with Decarli et al. (2016b, for a small subset of the sources).

The CO(1–0) observations cover all ASPECS sources between $z = 1.99$–2.70, except 1mm.C10, which lies outside of the VLA pointings (Section 2.3). The CO(1–0) fluxes measured here are consistent with Riechers et al. (2020), who measured the flux from the moment 0 maps collapsed over the channels in which emission was seen, while we obtain larger uncertainties compared to the optimized extractions. As all the lines are relatively faint (due to the apparently high r_{31}, see Section 5), this pushes the significance of some lines from $>3\sigma$ into the 2.5–3σ range (and are therefore not shown in Figure 2). For 3mm.7, the CO(1–0) line-shape is consistent with the CO(3–2), although the line is formally at 2.97σ in our fit. In other cases, the line width of the feature at the frequency of CO(1–0) appears different from the higher-J lines (e.g., 3mm.3, 3mm.12), which could be driven by the low S/N (see Riechers et al. 2020). An interesting case is 1mm.C14a, where the apparent CO(1–0) line appears offset both spatially and in velocity by $\sim$200 km s^{-1}, compared to the combined CO(6–5), CO(7–6), and [CI](2–1) lines. For this source we will use the fit results tied to the (formally undetected) CO(1–0) line for consistency, but note that if we only fit the other lines we find a slightly lower redshift solution ($z = 1.9963$) and higher S/N, such that the [C I](2–1) line is also at $>3\sigma$.

5. CO Excitation

5.1. Individual Sources

The CO line luminosities of all sources are shown in Figure 4 (in units of $L_\odot$) including both detections and 3σ upper limits. The ASPECS observations naturally divide the sample into different redshift bins, through the different low-, mid-, and high-J CO lines that are covered in Band 3 and Band 6 at different redshifts (Figure 1). For the galaxies from $z = 1.0$–1.6 ($\langle z\rangle = 1.2$), we measure the CO(2–1) line in Band 3 and either CO(4–3), CO(5–4), CO(6–5), and/or [C I](1−0) in Band 6, depending on the exact redshift. We cover both the CO(6–5) and CO(7–6) lines in the two sources at $z \approx 1.997$, but just miss the low-J CO(3–2) line in Band 3. For the higher

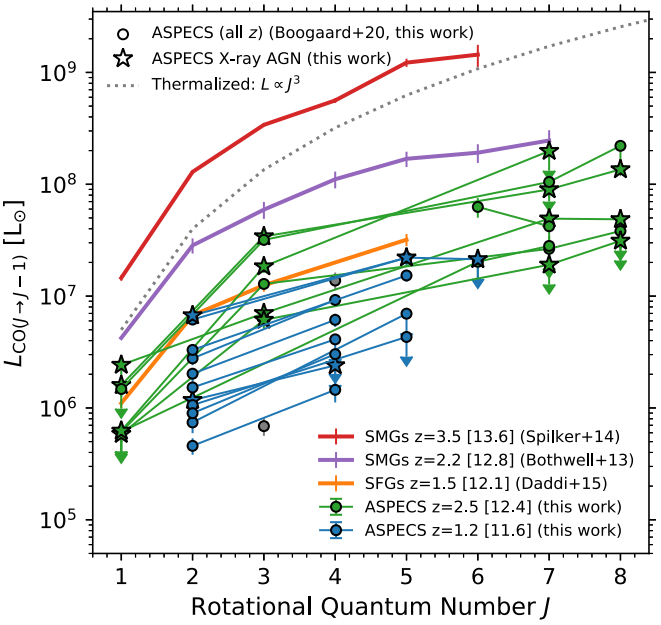

Figure 4. CO line luminosities (in units of $L_\odot$) of the ASPECS galaxies (colored circles). Downward pointing arrows indicate 3σ upper limits. Stars indicate X-ray sources classified as AGNs (Luo et al. 2017). For comparison, we show the average CO ladders of $\langle z\rangle = 1.5$ SFGs (Daddi et al. 2015) and submillimeter galaxies at $\langle z\rangle = 2.2$ (Bothwell et al. 2013) and $\langle z\rangle = 3.5$ (Spilker et al. 2014), and a thermalized ladder (arbitrarily scaled to 5×10^6 $L_\odot$). The average infrared luminosity ($\log L_{\rm IR}[L_\odot]$) of the different samples is indicated between brackets in the legend. Overall, the ASPECS galaxies probe lower infrared luminosities than typical samples at their respective redshifts.

redshift galaxies at $z = 2.4$–2.7, we cover CO(3–2) as well as CO(7–6), CO(8–7), and [C I](2−1). The VLA observations add constraints on CO(1–0) for all but one source at $z \geqslant 2$. Outside of these redshift bins we only have 1mm.C30 at $z = 0.46$ observed CO(3–2) in Band 6, for which we do not cover any other CO transition with ASPECS, and 3mm.13 at $z = 3.60$ for which we cover, but do not detect, CO(9–8) or CO(10–9).

We compare our observations to the average CO ladders from different samples in the literature: the BzK-selected SFGs at $\langle z\rangle = 1.5$ from Daddi et al. (2015); the SMGs at $\langle z\rangle = 2.2$ from Bothwell et al. (2013); and the stacked CO ladder for SPT-selected (lensed) SMGs at $\langle z\rangle = 3.5$ from Spilker et al. (2014). The ASPECS galaxies at $\langle z\rangle = 1.2$ are less massive and have a lower average infrared luminosity, $\langle L_{\rm IR}\rangle = 10^{11.6}$ $L_\odot$, than the BzK galaxies at $\langle z\rangle = 1.5$ ($10^{12.1}$ $L_\odot$). This is also clearly reflected in their overall lower CO luminosity. The ASPECS galaxies at $\langle z\rangle = 2.5$ also have a lower $\langle L_{\rm IR}\rangle = 10^{12.4}$ $L_\odot$ compared to the SMGs at similar redshifts.

We show the CO excitation ladders for the ASPECS galaxies at $\langle z\rangle = 1.2$ (left) and $\langle z\rangle = 2.5$ (right), relative to the low-J CO(2–1) and CO(3–2) transitions by which they were selected, respectively, in Figure 5 (now as line flux ratios). In addition to the $z > 1$ samples mentioned earlier, we also add the observed CO ladders for several local sources: the Milky Way (MW; Fixsen et al. 1999, Inner Disk) and starburst NGC 253 (Rosenberg et al. 2014), as well as the CO ladders for Arp 220 (Rangwala et al. 2011) and the nearest known quasar, Mrk 231 (van der Werf et al. 2010), as modeled by the LVG models of Weiß et al. (2007). The dotted line indicates a thermalized CO ladder (i.e., $S^V \propto J^2$).

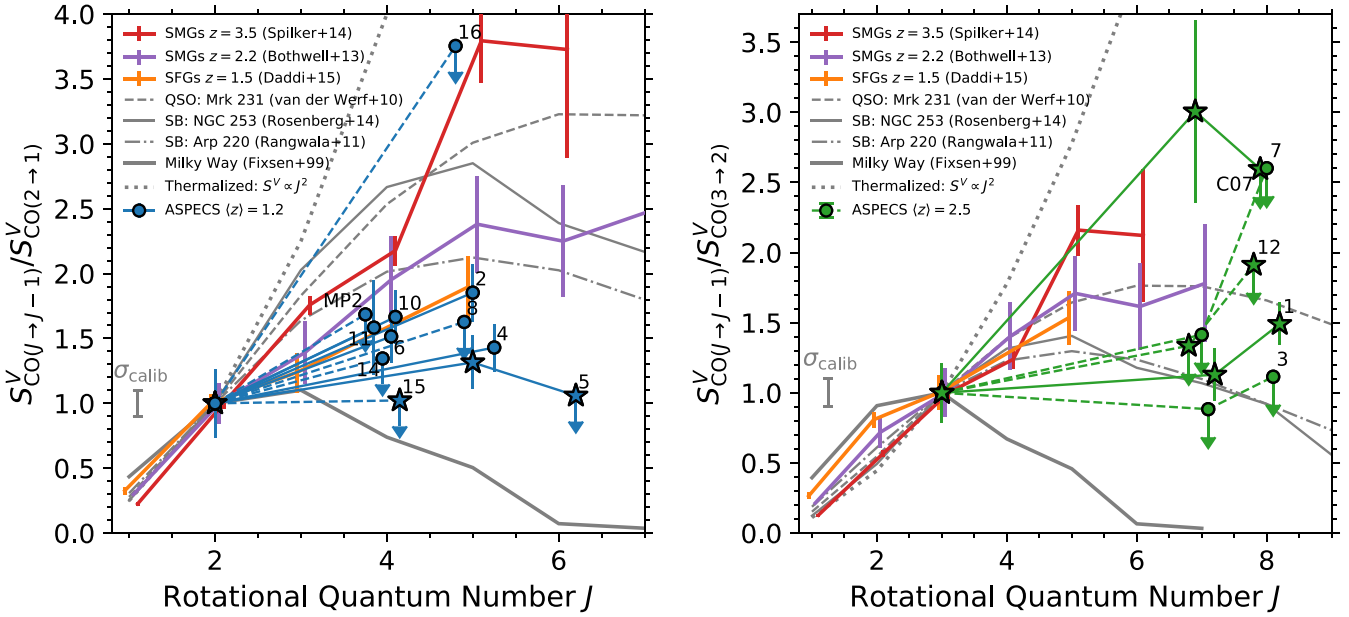

Figure 5. CO ladders for the ASPECS galaxies at $\langle z \rangle = 1.2$ (left) and $\langle z \rangle = 2.5$ (right), normalized to CO(2–1) and CO(3–2) respectively, in units of integrated line flux ($[S^V]$ = Jy km s^{-1}). We include all sources with coverage of at least two lines and a detection in the low-J line (except 3mm.09, which has a weakly constraining upper limit putting CO(7–6) just below the thermalized value). Downward pointing arrows indicate 3σ upper limits on the mid/high-J transition(s) and are connected to the lower-J transition with a dotted line. Stars indicate X-ray sources classified as AGNs (Luo et al. 2017). The gray error bar indicates the calibration uncertainty. The galaxies at $\langle z \rangle = 1.2$, show excitation in their mid-J lines, CO(4–3) and CO(5–4), that is consistent with, or lower than, what is found in the *BzK*-selected SFGs (Daddi et al. 2015). The range in excitation suggests that an additional, warmer, component is present in some, but not all, sources. At $\langle z \rangle = 2.5$, the excitation in the high-J lines, CO(7–6) and CO(8–7), is comparable to what is found in local starbursts (e.g., Rangwala et al. 2011; Rosenberg et al. 2014), but appears lower than the average sub-mm galaxy (Bothwell et al. 2013).

The 11 CO(2–1)-selected galaxies at $\langle z \rangle = 1.2$ (left panel) span a range in excitation in their CO(4–3) and CO(5–4) lines. Only one source (and one weak upper limit) show excitation in the CO(5–4) line that is comparable to the average of the *BzK*-selected SFGs (Daddi et al. 2015), while the other measurements and limits are consistent with lower excitation. We also add direct measurements of the CO(4–3) transition to this picture (which was not directly measured for the *BzK* galaxies). This ratio is similar to the (interpolated) value in the *BzK* galaxies for the three detected sources. At the same time we also infer upper limits consistent with lower excitation, although none of the sources have limits strong enough to put them confidently in the low-excitation regime of the MW. In all cases, the excitation is significantly lower compared to SMGs at higher redshift and clearly not as high as seen in the centers of the prototypical local starbursts Arp 220 and NGC 253, nor Mrk 231.

For the five CO(3–2) selected galaxies at $\langle z \rangle = 2.5$ (right panel), we probe the CO(7–6) and CO(8–7) lines. Here, we find the brightest galaxy of the survey (1mm.C01), which is an X-ray identified AGN with detections in all three lines (see Figure 3). This source exhibits significant excitation, out to $J = 8$, at the level comparable to the local starbursts and Mrk 231, though still somewhat below the $\langle z \rangle = 2.2$ SMGs at CO(7–6). There is one other source detected in CO(7–6), 1mm.C07, which is also an X-ray AGN. This source shows the highest r_{73} ratio of all sources, although we caution that the line flux is uncertain for both lines (see Figure 2) and the CO(8–7) transition is undetected. The remaining sources at these redshifts are not detected in their high-J lines. At the sensitivity limit of ASPECS, this constrains their high-J excitation to be well below thermalized and comparable to the level of the local starburst and somewhat below the Bothwell et al. (2013) SMGs.

We show the CO ladder normalized to CO(1–0) in Figure 6, for the sources with S/N > 3 in CO(1–0) in our joint fit. In contrast to the r_{73} ratio, the r_{31} ratio is typically higher than that of the Bothwell et al. (2013) SMGs.

The X-ray radiation from an AGN can drive the emission of the high-J CO lines (e.g., Meijerink et al. 2007; van der Werf et al. 2010; Vallini et al. 2019). The stars in Figures 5 and 6 indicate X-ray identified AGNs (1mm.C05, C12 at $\langle z \rangle = 1.2$ and 1mm.C01, C07, C19, and 3mm.09 at $\langle z \rangle = 2.5$). It is interesting to note that both sources detected in the high-J CO(7–6) line are X-ray AGNs. However, the upper limits on the remaining galaxies do not distinguish them clearly from the detected sources. At $\langle z \rangle = 1.2$, the X-ray AGNs lie at the low-excitation end of the sample, which is consistent with the AGNs not strongly driving the mid-J lines. Based on the low number of sources, we are unable to draw strong conclusions here. However, the results are consistent with recent work that did not find statistically different excitation, up to CO(7–6), between galaxies with and without an active nucleus (e.g., Sharon et al. 2016; Kirkpatrick et al. 2019).

5.2. Stacked Line Fluxes

We construct an average CO ladder in each of the two redshift bins by stacking the CO lines in each transition. The advantage of stacking (compared to taking the average of the measured line fluxes) is that we can straightforwardly take all sources into account in a non-parametric way, regardless of whether they are detected in a specific transition or not. Before stacking, we first take out the intrinsic brightness variations in the sample by dividing their spectra by the integrated flux in the

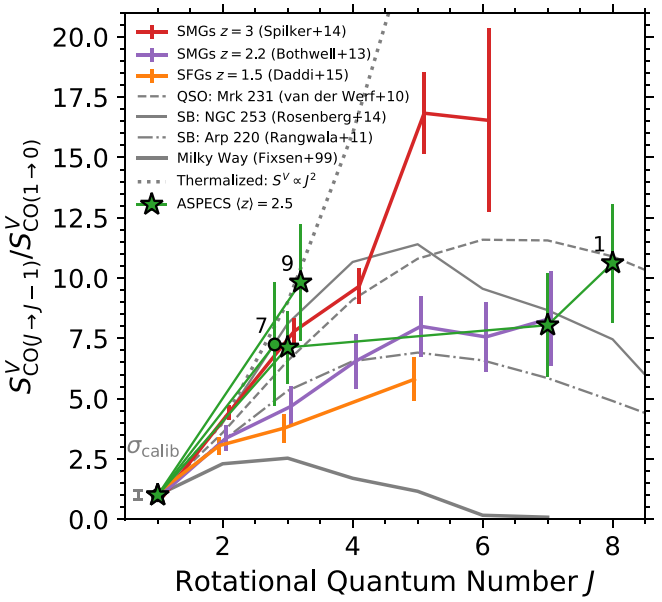

Figure 6. CO ladders of the ASPECS galaxies detected in CO(1–0) (green markers and lines), in units of integrated line flux ($[S^V] = \mathrm{Jy\,km\,s^{-1}}$), normalized to CO(1–0). Stars indicate X-ray sources classified as AGNs (Luo et al. 2017). The gray error bar indicates the combined calibration uncertainty on the ALMA and VLA data. The literature sample shown here is the same as shown in Figure 5. For all ladders, we propagate the uncertainty on the transition to which the ladders are normalized to the higher-J lines. We add slight offsets in the horizontal direction for clarity.

CO(2–1) or CO(3–2) transition (by which they were selected, depending on the redshift), as measured from the Gaussian fits. In this way we determine the average excitation of the other lines in the sample relative to CO(2–1) or CO(3–2) (including CO(1–0) and [C I]).

Because we are stacking sources with different line widths, care must be taken not to lose flux, while keeping an optimal S/N in the stack. Therefore, we stack each transition individually in velocity space, such that all the flux ends up in a single channel in the final stack (see Spilker et al. 2014). We first create a grid of velocities centered around zero. We take a channel width of 700 km s^{-1} for the sources at $\langle z \rangle = 1.2$ and 800 km s^{-1} for the sources at $\langle z \rangle = 2.5$, motivated by the width of the broadest lines in our sample (FWHM $\approx$ 590 and 660 km s^{-1} in each redshift bin, respectively). The average line width of the sample is $\langle \mathrm{FWHM} \rangle = 330$ km s^{-1}. At this channel width the CO(7–6) and [CI](2–1) lines, with a peak separation of 1000 km s^{-1}, are not blended in the stack. We find the results are robust to modifying the channel width by $\pm$100 km s^{-1}. After subtracting the continuum from the Band 6 spectra (as in Section 3.1), we convert each spectrum to velocity space, centered around the line. We then bin the spectra onto the velocity grid and stack them by taking the $1/\sigma$-weighted mean flux in each velocity bin (where σ is the rms error on the spectrum). Likewise, we determine the error spectrum of the stack by propagating the errors from individual spectra. We then measure the flux and error in the zero-velocity bin, which is centered on the line. We use a $1/\sigma$-weighting to avoid strongly weighting toward the detected lines, while at the same time not sacrificing too much S/N by not down-weighting very noisy spectra (as in an unweighted stack). Note this is different from Spilker et al. (2014), who use a $1/\sigma^2$-weighted stack to obtain the highest possible S/N.

Table 2
Average Line Fluxes from Stacking

Line (1)	N (2)	$S^V/S^V_{J=J_{\rm ref}}$ (3)	r_{JJ_l} (4)
$\langle z \rangle = 1.2$; $J_{\rm ref} = J_l = 2$			
CO(2–1)	11	1.00 ± 0.04	…
CO(4–3)	6	1.33 ± 0.18	0.33 ± 0.04
[C I](1–0)	8	0.33 ± 0.18	…
CO(5–4)	5	1.41 ± 0.15	0.23 ± 0.02
$\langle z \rangle = 2.5$; $J_{\rm ref} = 3$; $J_l = 1$			
CO(1–0)	6	0.14 ± 0.03	…
CO(3–2)	6	1.00 ± 0.03	0.77 ± 0.14
CO(7–6)	5	1.32 ± 0.18	0.19 ± 0.04
[C I](2–1)	5	0.93 ± 0.18	…
CO(8–7)	5	1.10 ± 0.20	0.12 ± 0.03

Note. The lines fluxes are obtained through $1/\sigma$-weighted stacking, scaled to the reference transition in the stack, with propagated errors. (1) Stacked transition (2) Number of objects in the stack of each transition. (3) Mean integrated line flux, normalized to the reference CO($J \rightarrow J-1$) transition in the stack, with $J = J_{\rm ref}$. (4) CO brightness temperature ratio with the lowest transition in the stack, $r_{JJ_l} = L'_{\rm CO(J\rightarrow J-1)}/L'_{\rm CO(J_l-J_l-1)}$.

The resulting line fluxes, normalized to the reference transition in the stack ($J_{\rm ref}$), are provided in Table 2, where we also report the line brightness temperature ratios (Equation (3)) to the lowest-J transition (J_l; note for the individual galaxies these are reported in Table 6). We show the average ladders, normalized to J_l, in Figure 7.

The stacks in the two redshift bins reinforce our results from Section 5.1. For the galaxies at $\langle z \rangle = 1.2$, excitation in the mid-J lines, compared to CO(2–1) is $r_{42} = 0.33 \pm 0.04$ and $r_{52} = 0.23 \pm 0.02$. This is on average lower than BzK-selected galaxies, in particular in CO(5–4) transition ($r_{52} = 0.30 \pm 0.06$; Daddi et al. 2015).[22] We now also add the recently published CO ladders for SFGs at $z = 1.25$ from Valentino et al. (2020a), who separate their sample in main-sequence galaxies and (extreme) starbursts (the latter being defined as lying a factor SFR/SFR$_{\rm MS} \geqslant 3.5\times$ and $\geqslant 7\times$ above the main sequence of Sargent et al. 2014). Their main-sequence galaxies show excitation intermediate between the BzK galaxies and ASPECS, with $r_{42} = 0.36 \pm 0.06$ and $r_{52} = 0.28 \pm 0.05$.

At $\langle z \rangle = 2.5$, we measure an average $r_{31} = 0.77 \pm 0.14$ from the stack of all sources. For comparison, when considering the non-detections as lower limits, the median of the individual measurements is 0.79 ± 0.17 (for 1mm.C01—fully consistent with 0.84 ± 0.18 as measured by Riechers et al. 2020). The stacked r_{31} value is higher than that found for SMGs by Bothwell et al. (2013, $r_{31} = 0.52 \pm 0.09$). At the same time, the high-J excitation, compared to $J = 3$ (r_{73}), is lower in our sample compared to Bothwell et al. (2013), as also seen in Figure 5. The mean $r_{71} = 0.19 \pm 0.04$ is similar to that of 1mm.C01 alone, and comparable to the SMGs ($r_{71} = 0.18 \pm 0.04$; Bothwell et al. 2013) and the local starburst NGC 253, while it lies below the local quasar Mrk 231 (see Section 5.1). Overall, the average ladder appears

[22] Daddi et al. (2015) did not measure the excitation in CO(4–3), but interpolating their CO ladder yields $r_{42} = 0.41 \pm 0.09$ (see Decarli et al. 2016b, for details).

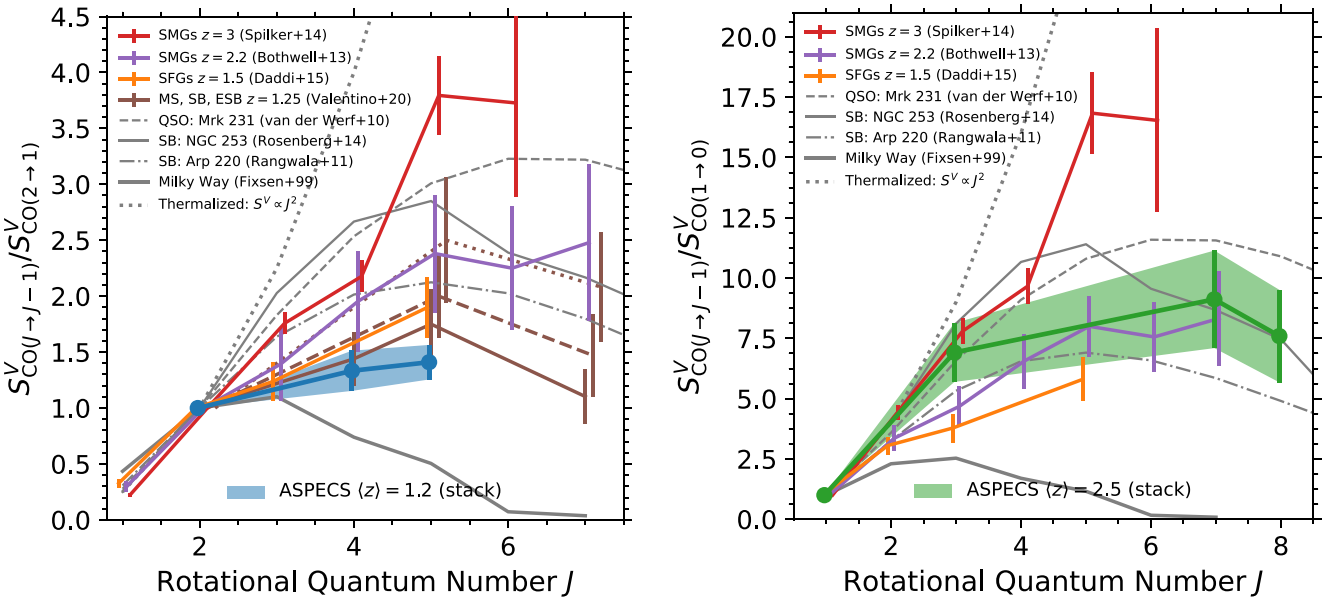

Figure 7. Average CO ladders for the ASPECS galaxies at $\langle z \rangle = 1.2$ (left) and $\langle z \rangle = 2.5$ (right), in units of integrated line flux ($[S^V] =$ Jy km s^{-1}), obtained through $(1/\sigma)$-weighted mean stacking after scaling to a common CO(2–1) and CO(3–2) flux, respectively. The solid line (and shaded region) show the mean stack of all sources. The literature sample shown here is the same as shown in Figure 5, with the addition of the recently observed main sequence and (extreme) starburst galaxies of Valentino et al. (2020a), shown by the brown, solid, and (dotted) dashed lines. For all ladders, we propagate the uncertainty on the transition to which the ladders are normalized to the higher-J lines. We add slight offsets in the horizontal direction for clarity.

similar to that found in local starburst galaxies, such as NGC 253.

In addition to stacking all sources selected in a certain transition, we also explored splitting the sample based on the presence of an AGN, or whether a line was individually (un) detected. We find marginal evidence of an overall lower excitation in the galaxies without an X-ray detected AGN at $\langle z \rangle = 2.5$ (in particular for the high-J lines), but the limited numbers in the stack prohibit firm conclusions.

5.3. LVG Modeling

To further investigate the CO excitation, we study the CO ladder of all sources at $z = 1.0$–1.6 and $z = 2.0$–2.7 in more detail by using a spherical, isothermal LVG model, following Weiß et al. (2007). Because we only observe up to four CO lines, we cannot accurately constrain the model parameters for individual sources. Rather, we use the model to predict the CO line luminosity of the neighboring, unobserved CO lines. The background to this approach is, that CO ladders cannot have arbitrary shapes and in this sense our procedure can be viewed as the molecular line correspondence of interpolating a sparsely sampled dust-continuum SED.

In practice, we fit the observed CO line luminosities using a one- and a two-component LVG model employing a Monte Carlo Bee algorithm (Pham & Castellani 2009) which samples randomly the parameter space and gives finer sampling for good solutions (evaluated from a χ^2 analysis for each model). The model-predicted CO line luminosities, $L'_{CO(J\rightarrow J-1)}$, and their uncertainties are calculated using the probability-weighted mean of all solutions and their standard deviations. For the redshift $z = 1.0$–1.6 sample, where we detect transitions up to $J = 5$, we report the model-predicted CO ladders up to $J = 6$. For the $z = 2.0$–2.7 sample we report transitions up to $J = 8$, because the observations also cover higher transitions. Typically, we investigate on the order of 10^6 models per galaxy. The free parameters are the H_2 volume density, the kinetic temperature, the CO abundance per velocity gradient, and the source solid angle (expressed as the equivalent radius of the emitting region, see Weiß et al. 2007). We include an additional prior that discards solutions where the peak of the CO ladder lies beyond the CO(7–6) line. This is motivated by our average ladder and there being only very few extreme local ULIRGs and $z = 2$–3 QSOs/SMGs where this is the case (see Weiss et al. 2007; Carilli & Walter 2013). Limits to the parameter space are: $\log_{10}(n_{H_2}) = 1.0$–7.0 cm^{-3}, $T_{kin} = 10$–200 K, $[CO]/[H_2](\Delta v/\Delta r)^{-1} = 10^{-3}$–$10^{-7}$(km s^{-1} pc^{-1})$^{-1}$ and $r_{eff} =$ 1–10 000 pc.

The CO ladders of the individual objects, derived from our single- and two-component LVG fitting, are shown in Figure 8, normalized to the predicted CO(1–0) line luminosity. We split the sample in two redshift bins, based on the observed lines (similar to Section 5.1). We also compute the average ladder in each redshift bin by computing the $1/\sigma$-weighted mean of the L'_{CO} for each of the lines, after first rescaling to a common $L'_{CO(1-0)}$ (to take out intrinsic variations in the luminosity). The resulting average ladders are provided in Table 3.

In general, the galaxies at $z \geqslant 2$ show more excited CO ladders than the galaxies at $z < 2$. This could partially be a selection effect in the case of the single-component models, if the fit overpredicts the $J = 3$ line luminosity in an attempt to fit $J > 6$, as suggested by the $r_{31} = 0.92 \pm 0.17$ being slightly higher than the stacked value ($r_{31} = 0.77 \pm 0.14$). However, the two-component model at $z \geqslant 2$ is still higher in $J = 2$ and 3, compared to the single-component fit at $z < 2$ (i.e., the "maximal" value at $z < 2$), whereas the average $r_{31} = 0.80 \pm 0.14$ is fully consistent with the stacked value. This strongly suggests that there is a true, intrinsic difference in excitation in the CO(2–1)-selected sample at $z < 2$ compared to the CO(3–2)-selected sample at $z \geqslant 2$. As we constrain two low/mid-J lines at both redshifts ($J = 1$ and 3 at $z \geqslant 2$, and $J = 2$ and 4 at $z < 2$), these conclusions appear robust against the fact that we also probe higher-J lines at $z \geqslant 2$.

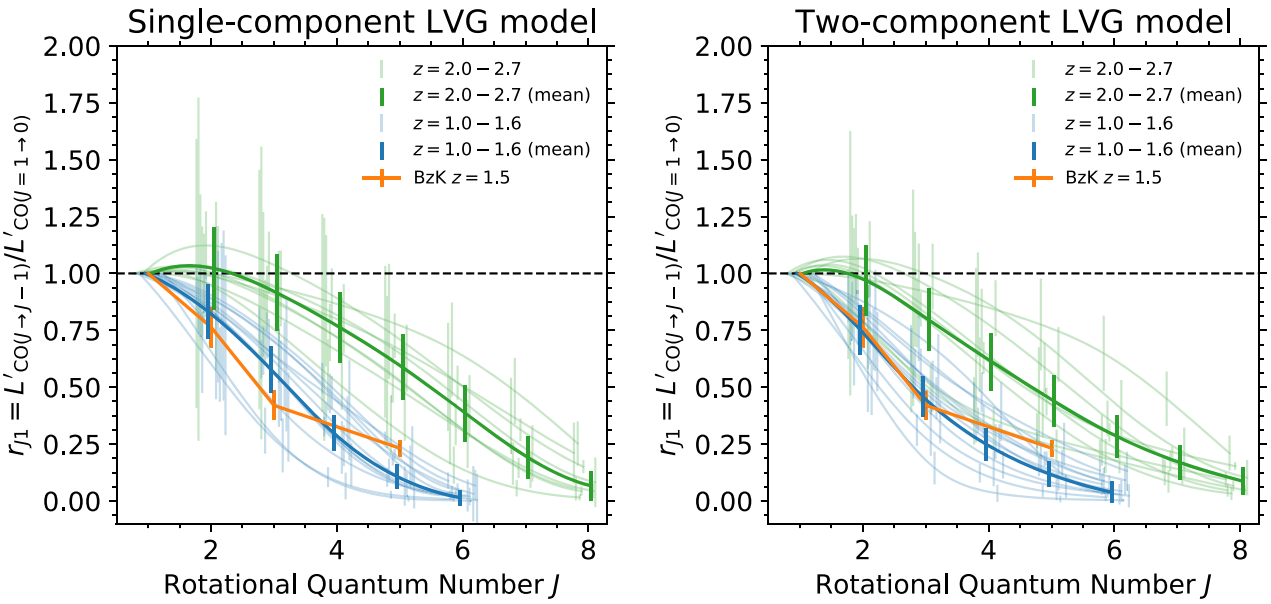

Figure 8. Predicted CO line luminosities ($L'_{CO(J \to J-1)}$) for the ASPECS galaxies at $z = 1.0$–1.6 and $z = 2.0$–2.7, normalized to $L'_{CO(1 \to 0)}$ (so the values on the ordinate are equivalent to r_{J1}). The CO line luminosities for the individual sources are predicted from the best-fit LVG model, assuming a single density and temperature component (left panel) as well as a two-component model (right panel). The light-colored lines show the individual fits, while the strong-colored line shows the $1/\sigma$-weighted mean of the individual ladders. While the temperature and density are degenerate in the fit, the emerging line luminosities are reasonably well constrained. We show the *BzK*-selected galaxies from Daddi et al. (2015) for comparison and add horizontal offsets for clarity. In both the single- and two-component models the CO(3–2) selected galaxies at $z = 2.0$–2.7 show on average higher excitation than the CO(2–1) selected galaxies at $z = 1.0$–1.6.

Table 3
LVG Modeling Results

	1-component		2-component[a]	
J (1)	$S^V/S^V_{J=1}$ (2)	r_{J1} (3)	$S^V/S^V_{J=1}$ (4)	r_{J1} (5)
		$z = 1.0$–1.6 (12 galaxies)		
1	1.00 ± 0.00	1.00 ± 0.00	1.00 ± 0.00	1.00 ± 0.00
2	3.33 ± 0.48	0.83 ± 0.12	3.01 ± 0.43	0.75 ± 0.11
3	5.20 ± 0.91	0.58 ± 0.10	4.12 ± 0.80	0.46 ± 0.09
4	4.76 ± 1.26	0.30 ± 0.08	4.01 ± 1.14	0.25 ± 0.07
5	2.70 ± 1.33	0.11 ± 0.05	2.99 ± 1.41	0.12 ± 0.06
6	0.53 ± 1.27	0.01 ± 0.04	1.37 ± 1.69	0.04 ± 0.05
		$z = 2.0$–2.7 (8 galaxies)		
1	1.00 ± 0.00	1.00 ± 0.00	1.00 ± 0.00	1.00 ± 0.00
2	4.09 ± 0.72	1.02 ± 0.18	3.88 ± 0.62	0.97 ± 0.15
3	8.24 ± 1.50	0.92 ± 0.17	7.17 ± 1.24	0.80 ± 0.14
4	12.21 ± 2.49	0.76 ± 0.16	9.80 ± 2.01	0.61 ± 0.13
5	14.68 ± 3.62	0.59 ± 0.14	10.95 ± 2.84	0.44 ± 0.11
6	13.86 ± 4.48	0.39 ± 0.12	10.17 ± 3.39	0.28 ± 0.09
7	9.33 ± 4.57	0.19 ± 0.09	8.28 ± 3.67	0.17 ± 0.07
8	4.26 ± 4.13	0.07 ± 0.06	5.55 ± 3.87	0.09 ± 0.06

Notes. The average line ratios are computed by taking the $1/\sigma$-weighted mean of the LVG models of the individual sources in each redshift bin. (1) CO($J \to J-1$) rotational quantum number J. (2) Single-component LVG model line flux, normalized to $J = 1$. (3) Single-component LVG model CO brightness temperature ratio, $r_{J1} = L'_{CO(J \to J-1)}/L'_{CO(1-0)}$. (4) Two-component LVG model line flux, normalized to $J = 1$. (5) Two-component LVG model CO brightness temperature ratio.
[a] We adopt the two-component models throughout this paper.

At $z = 1.0$–1.6, the single- and two-component models give formally consistent results, whereas the mean of the low-J lines is slightly higher for the single-component models ($r_{21} = 0.83 \pm 0.12$). The mean ladder of the two-component model is similar to the result from Daddi et al. (2015) for $J = 2$ and $J = 3$ ($r_{21} = 0.75 \pm 0.11$), while yielding a lower $J = 4$ and 5 (consistent with the stack). Although some individual sources show ladders consistent with thermalized $r_{21} = 1.0$ at these redshifts, the average is subthermal.

In general, we note that the single-component fits would overpredict the low-J excitation if the low-J CO line luminosities have a significant contribution from strongly subthermally excited gas. This is particularly significant at $z = 2.0$–2.7, as the $J > 6$ and $J \leqslant 3$ may not stem from the same component. However, this can also be important at $z = 1.0$–1.6, if the CO excitation is similar to the sources in Daddi et al. (2015) where the elevated $J = 5$ line luminosity is best described by a second, higher excitation component. This motivates the use of the two-component fit. In contrast, the observed CO transitions have little weight to constrain a two-component fit, in particular at $z = 1.0$–1.6, where we mostly only observe two CO transitions.

5.4. Dust Continuum versus Low-J CO

The 1.2 mm dust-continuum emission provides an alternative way of measuring the molecular gas mass, which is typically traced by the CO(1–0) emission (see Hildebrand 1983, for an early reference). Because the Rayleigh–Jeans tail of the dust emission is nearly always optically thin, the dust emission at long wavelengths is a direct probe of the total dust mass and therefore the molecular gas mass, under the assumption that the dust emissivity per unit dust mass and dust-to-gas ratio can be constrained (Scoville et al. 2014, 2016). Motivating a mass-weighted cold dust temperature $T_{dust} = 25$ K (which, in contrast to the light-weighted T_{dust}, is much less sensitive to the radiation field) and a dust emissivity index $\beta = 1.8$, Scoville et al. (2016) show that the observed ratio between the (inferred) dust luminosity at rest-frame 850 μm, L_ν (850 μm), and $L'_{CO(1-0)}$ is relatively constant under the wide range of

Table 4
ASPECS-LP Dust Continuum Data

ID 1mm	ID 3mm	z	S_ν(1.2 mm) (μJy)	S_ν(3 mm) (μJy)	L_ν(850 μm, rest)[a] (10^{29} erg s^{-1} Hz^{-1})	L_ν(850 μm, rest)[b] (10^{29} erg s^{-1} Hz^{-1})
(1)	(2)	(3)	(4)	(5)	(6)	(7)
1mm.C01	3mm.01	2.543	752 ± 24	32.5 ± 3.8	66.6 ± 2.1	47.4 ± 5.5
1mm.C03	3mm.04	1.414	429 ± 23	⩽20	41.3 ± 2.2	⋯
1mm.C04	3mm.03	2.454	316 ± 12	22.7 ± 4.2	28.3 ± 1.1	34.0 ± 6.3
1mm.C05	3mm.05	1.551	461 ± 28	27.4 ± 4.6	44.4 ± 2.7	52.0 ± 8.7
1mm.C06	3mm.07	2.696	1071 ± 47	46.5 ± 7.1	93.3 ± 4.1	64.8 ± 9.9
1mm.C07	⋯	2.58	233 ± 12	⩽20	20.5 ± 1.0	⋯
1mm.C09	3mm.13	3.601	155 ± 10	⩽20	12.4 ± 0.8	⋯
1mm.C10	⋯	1.997	342 ± 34	⩽20	32.1 ± 3.2	⋯
1mm.C12	3mm.15	1.096	114 ± 11	⩽20	10.5 ± 1.0	⋯
1mm.C13	3mm.10	1.037	116 ± 16	⩽20	10.6 ± 1.4	⋯
1mm.C14a	⋯	1.999	96 ± 10	⩽20	9.0 ± 0.9	⋯
1mm.C16	3mm.06	1.095	143 ± 18	⩽20	13.2 ± 1.6	⋯
1mm.C15	3mm.02	1.317	118 ± 13	⩽20	11.3 ± 1.3	⋯
1mm.C19	3mm.12	2.574	85 ± 12	⩽20	7.5 ± 1.1	⋯
1mm.C20	⋯	1.093	94 ± 16	⩽20	8.7 ± 1.5	⋯
1mm.C25	3mm.14	1.098	90 ± 17	⩽20	8.3 ± 1.6	⋯
1mm.C23	3mm.08	1.382	148 ± 30	⩽20	14.2 ± 2.9	⋯
1mm.C30	⋯	0.458	34 ± 10	⩽20	1.8 ± 0.5	⋯
⋯	3mm.11	1.096	⩽50	⩽20	⋯	⋯
…[c]	3mm.09	2.698	924 ± 76	44.5 ± 9.7	80.5 ± 6.6	62.0 ± 13.5
Faint.1mm.C20	3mm.16	1.294	86 ± 24	⩽20	8.2 ± 2.3	⋯
⋯	MP.3mm.2	1.087	⩽50	⩽20	⋯	⋯

Notes. (1) ASPECS-LP continuum ID (Aravena et al. 2020; González-López et al. 2020). (2) ASPECS-LP line ID (Boogaard et al. 2019). (3) Redshift. (4) Flux density at 1.2 mm (Aravena et al. 2020; González-López et al. 2020). (5) Flux density at 3 mm (González-López et al. 2019). (6) Rest-frame 850 μm luminosity density inferred from S_ν(1.2 mm), assuming $T_{\rm dust} = 25$ K and $\beta = 1.8$. (7) Rest-frame 850 μm luminosity density inferred from S_ν(3 mm), assuming $T_{\rm dust} = 25$ K and $\beta = 1.8$.

[a] Derived from S_ν(1.2 mm).

[b] Derived from S_ν(3 mm).

[c] Object falls outside of the Band 6 mosaic, but is the brightest 1 mm continuum source in the ASPECS field. We adopt the S_ν(1.3 mm) from Dunlop et al. (2017).

conditions found in local SFGs, (U)LIRGS, and (mostly lensed) SMGs. Recently, this has been further confirmed for a sample of $z \sim 2$ SFGs (Kaasinen et al. 2019) as well as simulations (Liang et al. 2018; Privon et al. 2018).[23]

We can thus investigate whether our galaxies (that are observed in $L'_{\rm CO(1-0)}$) follow the empirical relation with L_ν(850 μm) by Scoville et al. (2016), by directly comparing to their calibration sample. We then use it to place constraints on the excitation for the sources only observed in higher low-J lines. The advantage of this approach (rather than comparing inferred gas masses) is that it is independent of $\alpha_{\rm CO}$ and only depends on the assumed excitation correction (Equation (3)). Furthermore, we need not assume a gas-to-dust ratio, as this is implicit in the empirical correlation (but it does depend on the assumptions for $T_{\rm dust}$ and β, mentioned above). We stress that we cannot infer individual excitation corrections in this manner, since the calibration only holds on average and has a certain degree of intrinsic scatter.[24]

We estimate the rest-frame L_ν(850 μm) for our sources from the 1.2 mm continuum emission, assuming $T_{\rm dust} = 25$ K and $\beta = 1.8$ (Table 4). While a $T_{\rm dust} = 25$ K is arguably a good assumption for the cold dust that traces the cold gas mass (Scoville et al. 2016), we note that the observed SED, which should be used to scale the flux density to rest-frame 850 μm, is dominated by the luminosity-weighted dust temperature, which is likely higher. However, we adopt $T_{\rm dust} = 25$ K in order to remain consistent with the calibration sample of Scoville et al. (2016). We show the L_ν(850 μm) against the CO(1–0) luminosity in Figure 9. The ASPECS galaxies probe fainter dust luminosities than the calibration sample(s) at high-z. For the sources observed in CO(1–0), we find that the three detections (including 3mm.07) and the upper limits are consistent with the Scoville et al. (2016) relation. In Figure 10 (left panel), we show the same ratio, but with the $L'_{\rm CO}$ inferred from the low-J CO lines. Using $r_{21} = 0.75 \pm 0.11$ (Section 5.3), we find that the sources detected in CO(2–1) at $\langle z \rangle = 1.2$ on average lie relatively low compared to the Scoville relation, although several individual sources follow it well. Using the mean $r_{31} = 0.77 \pm 0.14$ (measured from stacking, Section 5.2) for the galaxies at $z = 2.0$–2.7, we find that most sources are consistent with the relation, including the galaxies not individually detected in CO(1–0), although the sample average is slightly below the relation. Assuming that the rest-frame 850 μm and CO luminosities are tightly correlated, this would suggest that the excitation values we adopt are too low on average, in particular for CO(2–1). For comparison, we also show the case in which the low-J lines are thermalized on average ($r_{21} = r_{31} = 1.0$;

[23] Motivated by their observed correlation between L_ν(850 μm) and $L'_{\rm CO(1-0)}$, Scoville et al. (2016) then empirically calibrate the $L_{\rm dust}$-to-$M_{\rm mol}$ ratio, assuming a CO-to-H_2 mass conversion factor of $\alpha_{\rm CO} = 6.5$ $M_\odot$ (K km s^{-1} pc^2)$^{-1}$ (incl. He). Note that, therefore, this estimate cannot be used to derive $\alpha_{\rm CO}$ independently.

[24] Using the data from Scoville et al. (2016), we measure a scatter around the relation of about 0.2 dex. However, this includes the scatter due to measurement and extrapolation errors (which are not provided in the paper), therefore the intrinsic scatter is potentially smaller.

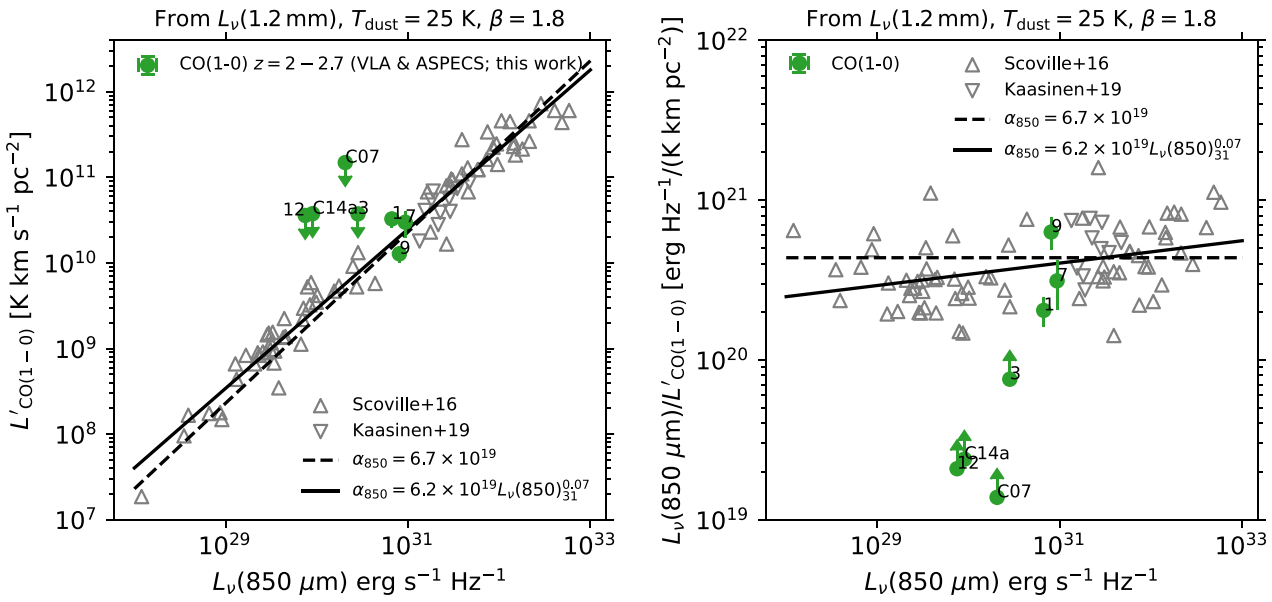

Figure 9. Rest-frame luminosity at 850 μm compared to the CO(1–0) luminosity (left) and the ratio of $L_\nu(850\ \mu{\rm m})/L'_{\rm CO(1-0)}$ (right). The CO(1–0) observations were taken with the VLA (Riechers et al. 2020) and are re-analyzed in this paper. Sources are indicated by the 3mm.ID (except 1mm.C07 and 1mm.C14a). The black lines show the best-fit empirical relations from Scoville et al. (2016; assuming both a constant and dust-luminosity dependent dust-to-gas conversion factor), while the gray triangles show their calibration sample as well as more recent observations from Kaasinen et al. (2019).

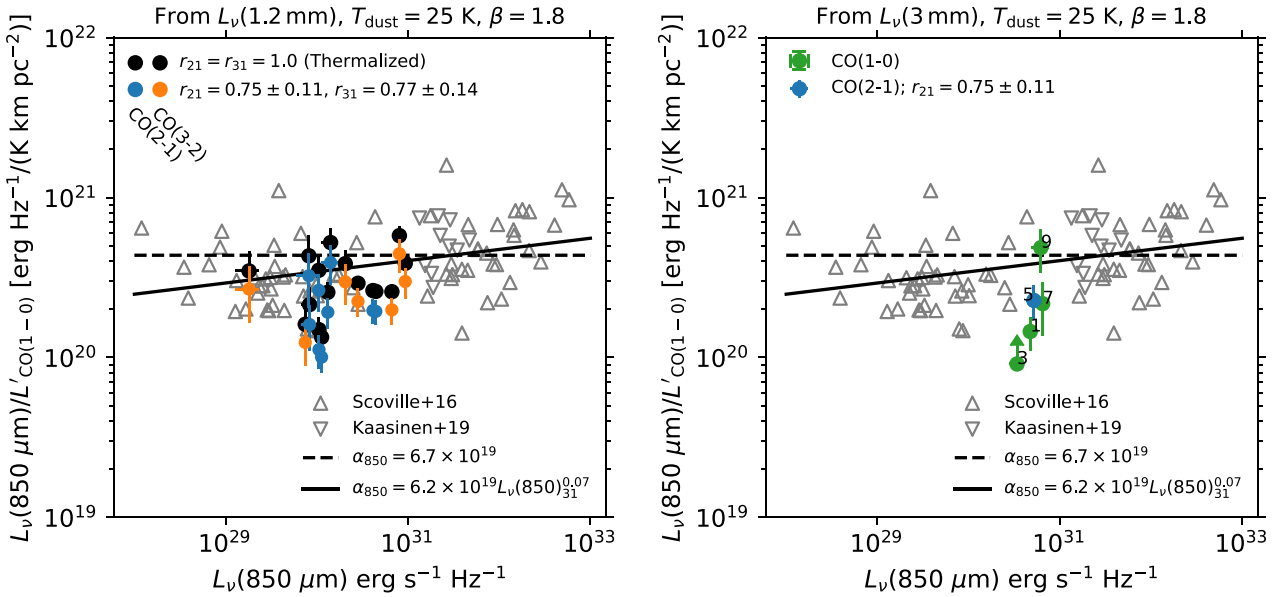

Figure 10. Left: the same as Figure 9 (right), but now using the inferred measurements of CO(1−0) from the low-J CO(2–1) and CO(3–2) lines, using the excitation corrections from Section 5.2. Right: the same as Figure 9 (right), but now the L_ν(850 μm) is inferred from the observed 3.0 mm continuum instead (when detected). The 3.0 mm continuum probes further down the Rayleigh–Jeans tail and is therefore less sensitive to the extrapolation to rest-frame 850 μm. The latter yields a slightly lower L_ν(850 μm), but overall both methods give very consistent results.

black points). We find an overall better agreement assuming the lines are thermalized on average. Although we cannot constrain the $L'_{\rm CO(1-0)}$ for individual sources via the L_ν(850 μm) calibration, the comparison implies that, on average, the r_{21} and r_{31} may not be much lower than ∼0.75, on average, at $\langle z \rangle = 1.2$ and 2.5, respectively (consistent with the stacking and LVG modeling). Note that to make the CO and dust fully consistent with the empirical relation, based on CO excitation alone, would imply suprathermalized CO in some cases, which is not expected to occur under normal conditions in the ISM, where the CO is optically thick (but $r_{J1} > 1$ is possible if the CO is optically thin).

An alternative explanation for the low $L_\nu(850\ \mu{\rm m})/L'_{\rm CO}$ ratios is a bias due to the CO-selection. Comparing the primary, flux-limited samples (see Section 2.2) of both the CO and dust-continuum-selected sources with a redshift at which we can

detect CO, we find that there are two CO(2−1)-selected sources without dust continuum and potentially[25] two vice versa. At the same time, all CO(3–2) emitters are detected in dust continuum, while there are potentially four dust-selected sources at $z = 2$–3 without CO(3–2). While the number of galaxies under consideration is modest, this argues against a strong selection effect, at least for the CO(2–1)-selected sources, in which case we would expect a larger number of dust-selected sources with CO emission (filling in the scatter above the relation). Because the CO detection limit increases relative to that of the dust continuum (as the latter experiences a strong negative k-correction, e.g., Blain et al. 2002), a selection effect is expected to be stronger for the CO(3–2)-selected sources, as is indeed suggested by the above comparison. However, the latter galaxies do not show systematically lower ratios, compared to the CO(2–1) selected sources, and direct observations of CO(1–0) for a few of the sources do not suggest a strong systematic offset. Overall, we therefore conclude that, while we cannot fully exclude the impact of selection, it does not appear to play a dominant role at least for the CO(2–1)-selected sources.

Finally, to investigate the influence of the Rayleigh–Jeans correction on the results (in particular for the higher redshift sources), we also infer $L_\nu(850\ \mu\mathrm{m})$ from the 3.0 mm continuum data, that has been detected in four of the galaxies at $z \approx 2.6$ and 3mm.05 at $z = 1.55$ (Figure 9, right panel). The rest-frame $L_\nu(850\ \mu\mathrm{m})$ luminosities inferred from 3.0 mm are on average ≈10% lower than those from the 1.2 mm, but overall we come to the same conclusions.

6. Atomic Carbon

6.1. Atomic Carbon Abundances

Atomic carbon has been suggested as a good alternative tracer of the molecular gas mass. This is motivated by the fact that the emission from atomic carbon ([C I]) has been found to be closely associated with CO emission in a range of different environments in the MW (Stutzki et al. 1997; Ojha et al. 2001; Ikeda et al. 2002; Schneider et al. 2003) and in local galaxies (e.g., Gerin & Phillips 2000; Israel et al. 2015; Jiao et al. 2019). There has been some debate to whether [C I] can be used to trace the total molecular gas mass, because the [C I] emission was originally predicted to arise only from a narrow [C II]/[C I]/CO transition zone in molecular clouds on the basis of early theoretical work (Tielens & Hollenbach 1985a, 1985b; see Israel et al. 2015). However, more recent models have supported the picture in which CO and [C I] coexist over a wide range of conditions (see, e.g., Papadopoulos et al. 2004; Bisbas et al. 2015, 2017; Glover et al. 2015).

The [C I] lines are typically found to be optically thin (Ojha et al. 2001; Ikeda et al. 2002; Weiß et al. 2003). As a result, the [C I] column density in the upper levels of the $^3P_2 \rightarrow {}^3P_1$ ($\nu_{\rm rest} = 809.342$ GHz) and $^3P_1 \rightarrow {}^3P_0$ ($\nu_{\rm rest} = 492.161$ GHz) transitions is directly related to the line intensity, and depends only on the excitation temperature, $T_{\rm ex}$ (e.g., Frerking et al. 1989; Stutzki et al. 1997; Weiß et al. 2003, given their low critical densities, $<10^3$ cm^{-3}). This means that the atomic carbon mass ($M_{\rm [C\,I]}$) can be directly inferred from the line luminosity:

$$M_{\rm [CI]} = 5.706 \times 10^{-4} Q(T_{\rm ex}) \frac{e^{T_1/T_{\rm ex}}}{3} L'_{\rm [C\,I](1\text{-}0)}\ M_\odot \quad (5)$$

$$M_{\rm [CI]} = 4.556 \times 10^{-4} Q(T_{\rm ex}) \frac{e^{T_2/T_{\rm ex}}}{5} L'_{\rm [C\,I](2\text{-}1)}\ M_\odot. \quad (6)$$

Here, $T_1 = 23.6$ K and $T_2 = 62.5$ K are the energies of the $^3P_2$ and $^3P_1$ levels and $Q(T_{\rm ex}) = 1 + 3e^{-T_1/T_{\rm ex}} + 5e^{-T_2/T_{\rm ex}}$ is the partition function in the three-level system approximation (Weiß et al. 2003, 2005).

The excitation temperature itself can be measured directly from the ratio of the integrated line intensities,

$$T_{\rm ex} = \frac{38.8\ \mathrm{K}}{\ln(2.11/R)}, \quad (7)$$

where $R = L'_{\rm [C\,I](2-1)}/L'_{\rm [C\,I](1-0)}$ (Stutzki et al. 1997). Walter et al. (2011) measured an excitation temperature of $\langle T_{\rm ex}\rangle = 29.1 \pm 6.3$ K in a sample of $\langle z\rangle = 2.5$ SMGs. As we never observe both [C I] transitions in the same source, we assume a typical value of $T_{\rm ex} = 30$ K (see Weiß et al. 2005; Bothwell et al. 2017; Popping et al. 2017; Valentino et al. 2018; Brisbin et al. 2019, corresponding to $R = 0.58$). Note from Equations (5) and (6) that the neutral atomic carbon mass is not a strong function of the assumed excitation temperatures above ≈20 K for [C I](1–0) and ≈40 K for [C I](2–1) (as pointed out by Weiß et al. 2005).

Before turning to the masses inferred from [C I] and CO, we compare the line luminosities directly, as a function of $L_{\rm IR}$, in the left panel of Figure 11. In particular at $\langle z\rangle = 1.2$, we probe [C I] in galaxies at lower $L_{\rm IR}$ than previous studies of similar sources. Overall, the ratios are comparable to those in the main-sequence galaxies from Valentino et al. (2018) and the average ratio in a variety of local galaxies from Gerin & Phillips (2000).

We derive [C I] masses of a few $\times 10^6\ M_\odot$ (Table 5). From the [C I] masses, we derive the galaxy average, luminosity-weighted, neutral atomic carbon abundances,

$$\frac{[\mathrm{C\,I}]}{[\mathrm{H_2}]} = \frac{M_{\rm [C\,I]}}{6M_{\rm H_2}}, \quad (8)$$

where $M_{\rm H_2} = M_{\rm mol}/1.36$, not including He. We use the CO-derived $\mathrm{H_2}$ masses, adopting $r_{21} = 0.75 \pm 0.11$ and $r_{31} = 0.77 \pm 0.14$ for the sources without CO(1–0), and $\alpha_{\rm CO} = 3.6\ M_\odot\ (\mathrm{K\,km\,s^{-1}\,pc^2})^{-1}$. The abundances are shown as a function $L_{\rm IR}$ in Figure 11. We find an average abundance of $([\mathrm{C\,I}]/[\mathrm{H_2}])_{\rm CO} = (1.9 \pm 0.4) \times 10^{-5}$ (ignoring limits).[26] Overall, the abundances are broadly similar to those in the MW (2.2×10^{-5}, Frerking et al. 1989) and in $z \approx 1.2$ main-sequence galaxies ($(1.6 \pm 0.8) \times 10^{-5}$; Valentino et al. 2018), but lower than in high-redshift SMGs (Walter et al. 2011; Alaghband-Zadeh et al. 2013; Bothwell et al. 2017). However, as pointed out by Valentino et al. (2018), these differences could also be driven by the difference in adopted $\alpha_{\rm CO}$, as their derived abundances assume an $\alpha_{\rm CO} = 0.8\ M_\odot(\mathrm{K\,km\,s^{-1}\,pc^2})^{-1}$, which is the typical value assumed for these systems. Finally, we come to similar

[25] The precise number is dependent on the accuracy of the redshift measurement available for the dust-continuum sources.

[26] If we instead assume thermalized CO for all sources without CO(1–0), we derive $([\mathrm{C\,I}]/[\mathrm{H_2}])_{\rm CO} = (2.2 \pm 0.4) \times 10^{-5}$.

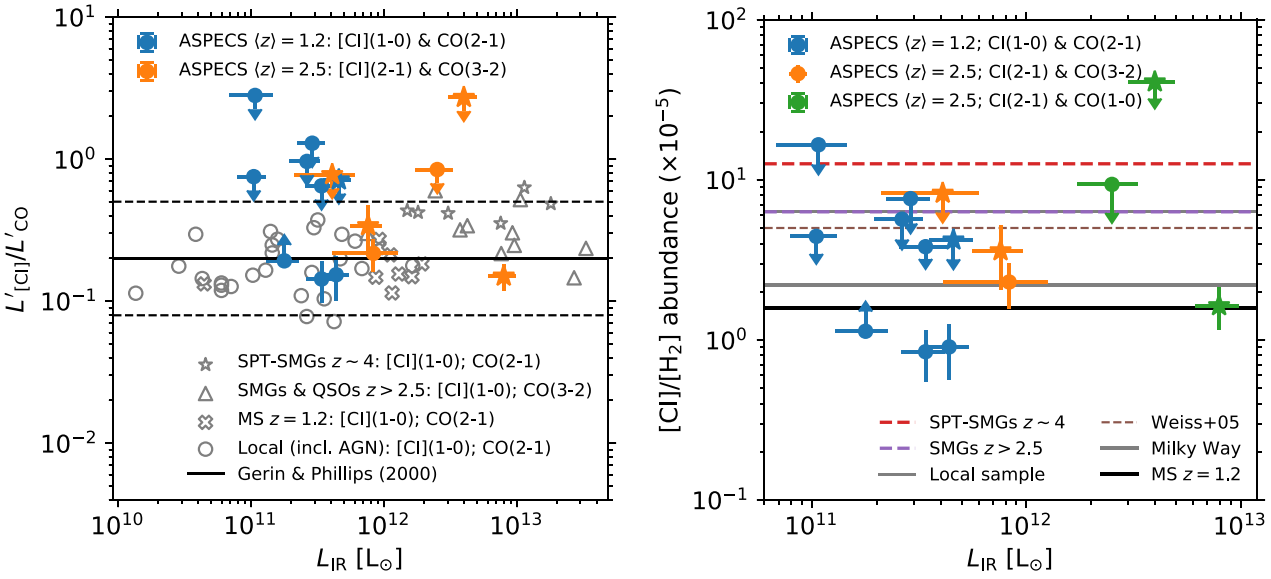

Figure 11. Left: $L_{[\mathrm{C\,I}]}/L'_{\mathrm{CO}}$ ratio for [C I]($^3P_1 \rightarrow {}^3P_0$) over CO(2–1) (blue) and [C I]($^3P_2 \rightarrow {}^3P_1$) over CO(3–2) (orange), where stars indicate X-ray AGNs. We compare the observed ratios to SPT-SMGs at $z = 4$ (Bothwell et al. 2017), SMGs at $z \geqslant 2.5$ (Walter et al. 2011; Alaghband-Zadeh et al. 2013), main-sequence galaxies at $z = 1.2$ and local galaxies, as compiled by Valentino et al. (2018), and the average ratio and scatter in the local sample from Gerin & Phillips (2000). Overall, the ratios broadly agree with the spread found for previous samples of SFGs. Right: atomic carbon abundance in the ASPECS galaxies. The H_2 mass was derived from CO(2–1) (assuming $r_{21} = 0.75 \pm 0.11$) and CO(1–0) or CO(3–2) (assuming $r_{31} = 0.77 \pm 0.14$), with $\alpha_{\mathrm{CO}} = 3.6\ M_\odot(\mathrm{K\ km\ s^{-1}\ pc^2})^{-1}$, for the galaxies detected in [C I](1–0) and [C I](2–1), respectively. We compare our measurements to the abundances for different galaxy types (excluding active galaxies), converted to a common α_{CO} by Valentino et al. (2018). On average we find [C I] abundances similar to the MW (Frerking et al. 1989) and the SFGs from Valentino et al. (2018) (who assumes a galaxy-specific α_{CO}, which is 3.0 on average, and $r_{21} = 0.84$), with higher abundances at $\langle z \rangle = 2.5$ compared to $\langle z \rangle = 1.2$. Note that the higher abundances in the submillimeter galaxies from literature are partly driven by the assumed lower α_{CO} in these systems.

Table 5
Masses from Different Tracers and Neutral Atomic Carbon Abundances for the [C I] Detected Galaxies

ID	z	$M_{\mathrm{mol,RJ}}$ ($\times 10^{10}\ M_\odot$)	$M_{\mathrm{mol,CO}}$ ($\times 10^{10}\ M_\odot$)	$M_{[\mathrm{C\,I}]}$ ($\times 10^{6}\ M_\odot$)	$([\mathrm{C\,I}]/[\mathrm{H_2}])_{\mathrm{RJ}}$ ($\times 10^{-5}$)	$([\mathrm{C\,I}]/[\mathrm{H_2}])_{\mathrm{CO}}$ ($\times 10^{-5}$)
(1)	(2)	(3)	(4)	(5)	(6)	(7)
1mm.C12	1.09	1.6 ± 0.2	1.4 ± 0.3	$\leqslant 2.7$	$\leqslant 3.8$	$\leqslant 4.2$
1mm.C13	1.03	1.6 ± 0.2	3.4 ± 0.7	1.4 ± 0.4	1.9 ± 0.7	0.9 ± 0.3
1mm.C16	1.09	2.0 ± 0.2	2.5 ± 0.4	0.9 ± 0.3	1.1 ± 0.4	0.8 ± 0.3
1mm.C15	1.31	1.7 ± 0.2	4.0 ± 0.7	$\leqslant 6.8$	$\leqslant 9.1$	$\leqslant 3.8$
1mm.C20	1.09	1.3 ± 0.2	$\leqslant 3.3$	1.6 ± 0.5	2.9 ± 1.0	$\geqslant 1.1$
1mm.C25	1.09	1.3 ± 0.2	1.9 ± 0.5	$\leqslant 4.7$	$\leqslant 8.5$	$\leqslant 5.7$
3mm.11	1.09	$\leqslant 0.4$	0.6 ± 0.1	$\leqslant 1.1$	...	$\leqslant 4.4$
3mm.16	1.29	1.2 ± 0.3	0.9 ± 0.2	$\leqslant 6.6$	$\leqslant 12.3$	$\leqslant 16.5$
MP.3mm.2	1.09	$\leqslant 0.4$	1.1 ± 0.3	$\leqslant 3.7$	$\leqslant 20.2$	$\leqslant 7.6$
1mm.C01	2.54	10.0 ± 0.3	11.7 ± 2.4	8.5 ± 1.8	1.9 ± 0.4	1.6 ± 0.5
1mm.C04[a]	2.45	4.2 ± 0.2	4.5 ± 0.9	4.6 ± 1.1	2.5 ± 0.6	2.3 ± 0.7
1mm.C06	2.69	14.0 ± 0.6	10.7 ± 3.6	$\leqslant 44.3$	$\leqslant 7.2$	$\leqslant 9.4$
1mm.C07[a]	2.58	3.1 ± 0.2	2.5 ± 0.7	3.9 ± 1.3	2.9 ± 1.0	3.6 ± 1.6
1mm.C19[a]	2.57	1.1 ± 0.2	2.2 ± 0.5	$\leqslant 7.3$	$\leqslant 16.0$	$\leqslant 8.2$
3mm.9	2.70	12.0 ± 1.0	4.6 ± 1.0	$\leqslant 83.1$	$\leqslant 15.6$	$\leqslant 40.9$

Notes. Properties derived for [C I](1–0) and CO(2–1) at $1 \leqslant z < 2$, assuming $r_{21} = 0.75 \pm 0.11$ (top rows) and from [C I](2–1) and CO(1–0), or CO(3–2) assuming $r_{31} = 0.77 \pm 0.14$, at $2 \leqslant z < 3$ (bottom rows). In the case of a non-detection we report a 3σ upper limit. (1) ASPECS-LP ID (see Table 1). (2) Redshift. (3) Molecular gas mass determined via the 1.2 mm dust-continuum emission on the Rayleigh–Jeans tail (Section 5.4; see Table 4). (4) Molecular gas emission determined from the CO line luminosity emission assuming $\alpha_{\mathrm{CO}} = 3.6\ M_\odot(\mathrm{K\ km\ s^{-1}\ pc^2})^{-1}$ (Equation (4)). (5) Atomic carbon mass derived from [C I](1–0) and [C I](2–1) via Equations (5) and (6). (6) Neutral atomic carbon abundance computed with $M_{\mathrm{mol,RJ}}$ (Equation (8)). (7) Neutral atomic carbon abundance, computed with $M_{\mathrm{mol,CO}}$.
[a] CO related properties derived from CO(3–2) assuming $r_{31} = 0.77 \pm 0.14$.

conclusions if we use the dust continuum based molecular gas masses instead, $([\mathrm{C\,I}]/[\mathrm{H_2}])_{\mathrm{RJ}} = (2.2 \pm 0.3) \times 10^{-5}$, assuming the luminosity independent calibration from Scoville et al. (2016) (Section 5.4).

6.2. PDR Modeling

We use the combination of [C I], CO and far-infrared dust emission (L_{IR}) to explore the ISM properties of the galaxies in our sample using PDR models. To this end, we use the results

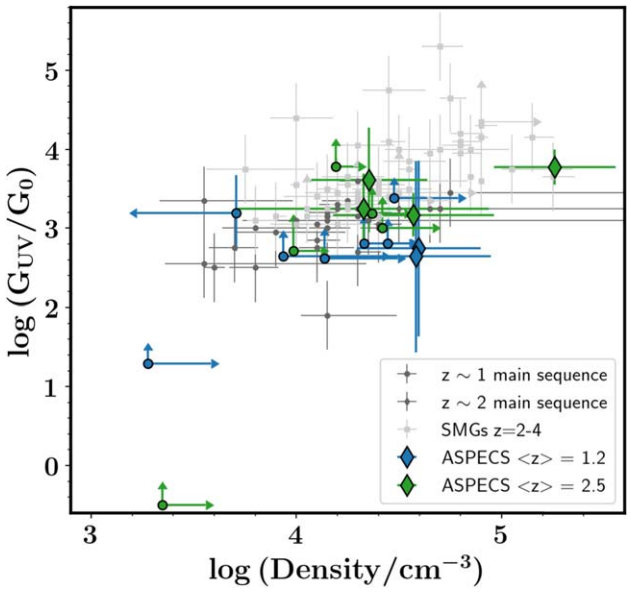

Figure 12. ISM density and UV radiation field strength ($G_{\rm UV}$, relative to the local galactic interstellar radiation field, G_0; Habing 1968) as inferred from PDR modeling. The ASPECS galaxies are shown as diamonds or, in the case of a limit on either parameter, circles. These galaxies are compared to main-sequence galaxies at $z \sim 1$ (Valentino et al. 2018, 2020b; Bourne et al. 2019) and $z \sim 2$ (Popping et al. 2017; Talia et al. 2018) and $z = 2$–4 SMGs (Walter et al. 2011; Alaghband-Zadeh et al. 2013; Bothwell et al. 2017; Yang et al. 2017; Andreani et al. 2018; Cañameras et al. 2018; Harrington et al. 2018; Dannerbauer et al. 2019; Nesvadba et al. 2019; Jin et al. 2019) for which Valentino et al. (2020b) re-derived the density and UV radiation field (using similar lines and model assumptions as in this paper).

from the PDRTOOLBOX (Kaufman et al. 2006; Pound & Wolfire 2008). The PDRTOOLBOX is based on the one-dimensional models from Kaufman et al. (2006) and solves for the chemistry, thermal balance, and radiative transfer, assuming metal, dust, and polycyclic aromatic hydrocarbon abundances and a gas microturbulent velocity. Every PDR is described by a fixed number density of H nuclei and intensity of the impinging UV radiation field, $G_{\rm UV}$, in units of the local galactic interstellar radiation field, G_0 (Habing 1968). The PDRTOOLBOX then provides the line ratio of [CI], CO and $L_{\rm IR}$ as a function of the density and UV radiation field of a PDR.

We estimate the ISM density and UV radiation field by using a combination of the [C I] and CO emission lines for each galaxy. We specifically focus on CO emission from rotational transitions equal to or lower than CO(4–3), unless these are not available, as higher order CO emission originates from significantly denser ISM than [C I] (see Valentino et al. 2020b). We adopt a numerical approach where we bootstrap the observed flux ratios within their error 1000 times and solve for the ISM density and UV radiation field for each instance. As the final density and radiation field we take the median of these values. The 68% confidence interval is taken as the error on the derived values. For the non-detected lines we run the models using 3σ upper limits on the line fluxes and interpret the results as lower or upper limits accordingly. Similar analyses have been performed in, for instance, Alaghband-Zadeh et al. (2013), Bothwell et al. (2017), Popping et al. (2017), Cañameras et al. (2018), Brisbin et al. (2019), and Valentino et al. (2020b).

The results of the PDR modeling are shown in Figure 12. In general, we find that the PDR models predict fairly high densities, $\geqslant 10^4$ cm^{-3}, for all sources. In the PDR model, this is constrained by the ratio of [C I] (with low critical density) over CO. The UV radiation field strength is primarily determined by the ratio of the lines over the dust continuum and found to be $\geqslant 3 \times 10^2$ G_0 in most cases. The median $G_{\rm UV}$ of the detections appears to be larger at $\langle z \rangle = 2.5$ compared to $\langle z \rangle = 1.2$ in our sample, though this difference is not statistically significant. Overall, the galaxies occupy the same parameter space as the main-sequence galaxies from Valentino et al. (2018, 2020b), who also modeled the CO and [C I] lines.

We note that the PDR model adopted in this analysis (and other works) assumes that the ISM of a galaxy can be described by a single PDR with a fixed input abundance. In reality, the ISM consists of a range of molecular clouds that all have different properties (density, impinging UV radiation field, abundances). Furthermore, the PDR models assume a fixed density throughout the medium, whereas in reality the density distribution of PDRs is more complex. Following Valentino et al. (2018), we also do not correct the models for the difference in optical depth between CO, [C I], and $L_{\rm IR}$, and therefore restrict our relative comparison with the literature to these data, which are consistently analyzed. Our results should therefore be treated as qualitative measures of the ISM density and UV radiation field. Alaghband-Zadeh et al. (2013), Bothwell et al. (2017), Cañameras et al. (2018), and Valentino et al. (2020b) discuss in more detail that the PDR modeling likely does not capture the full complexity of the ISM in galaxies and should be taken as an order of magnitude indication of the ISM properties. Future work attempting to model the ISM properties of galaxies should thus focus on spatially resolved observations and multiphase modeling of the ISM.

7. Discussion

7.1. Modest Excitation in Mid-J Lines at z = 1.0–1.6

The ASPECS galaxies significantly expand the sample of SFGs with CO excitation measurements at $z = 1.0$–1.6. In particular, our observations increase the number of detections of the CO(4–3) and CO(5–4) lines in sources at these redshifts. A key result of our study is that the $\langle z \rangle = 1.2$ galaxies, selected by their CO(2–1) emission, show a range in excitation of their $J \geqslant 2$ lines up to CO(5–4). In half of the sample we find that the mid-J CO lines are excited to similar (interpolated) levels as the *BzK* galaxies at $\langle z \rangle = 1.5$, suggesting the presence of a dense, warm component in the ISM of these galaxies (Daddi et al. 2015). However, the remaining galaxies are consistent with lower excitation, as shown by the average stacked ladder including the individually non-detected transitions as well (see Figure 5). This indicates that such a warm, dense component is not as dominantly present in all galaxies. On average, the ASPECS galaxies at $\langle z \rangle = 1.2$ are less excited in their mid-J lines compared to the *BzK* galaxies from Daddi et al. (2015), but, the average mid-J excitation is above that observed in, e.g., the MW.

The lower excitation of the ASPECS galaxies can be naturally explained by their lower surface density of star formation, as the excitation correlates with the radiative energy input into the gas. The CO excitation is sensitive to the gas density and temperature and is known to correlate with the dust temperature (Rosenberg et al. 2015) and radiation field strength, star formation efficiency and SFR surface density (Daddi et al. 2015; Valentino et al. 2020a). The excitation has

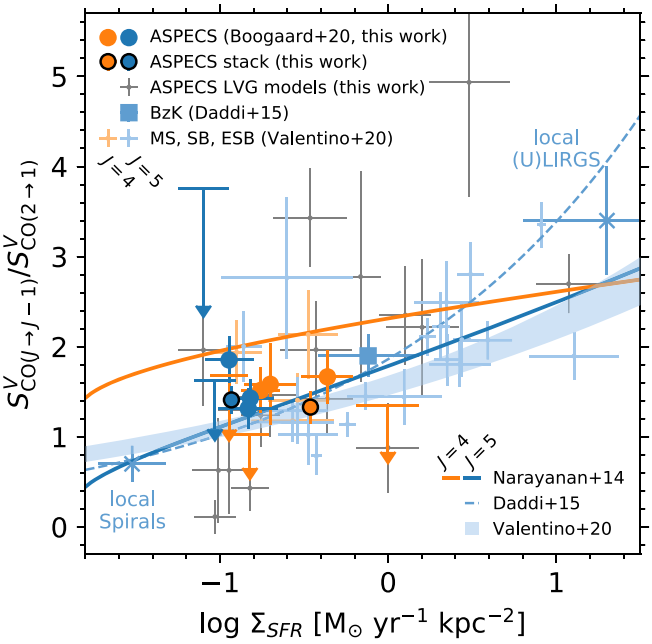

Figure 13. SFR surface density (Σ_{SFR}) vs. CO line flux ratio (in units of S^V), for both CO(4–3)/CO(2–1) (orange) and CO(5–4)/CO(2–1) (blue). The colored points (and limits) show the observed line flux ratios of the ASPECS galaxies, while the gray points show the predicted ratios from the LVG model fits for all galaxies (for CO(5–4)/CO(2–1) only; note the points are not visible for the galaxies in which we directly measure the ratio). We also show the values from the stacks (Section 5.2) at the mean Σ_{SFR}. The blue square shows the average of the BzK-selected SFGs from Daddi et al. (2015) and the blue crosses show averages for local spirals and (U)LIRGS as reported by Daddi et al. (2015). The light shaded points show the recent data for main-sequence and (extreme) starburst galaxies from Valentino et al. (2020a). The solid lines show the predictions from the Narayanan & Krumholz (2014) models for unresolved observations, the dashed blue line shows the best fit from Daddi et al. (2015) and the shaded region shows that from Valentino et al. (2020a) (for CO(5–4) only).

also been shown to correlate, to a lesser extent, with the L_{IR} (e.g., Rosenberg et al. 2015). The connection between L_{IR} and excitation is less direct, however, because the total SFR does not correlate with the density and temperature of the clouds as Σ_{SFR} does (see Narayanan & Krumholz 2014). This conclusion is also reached by Valentino et al. (2020a), who show that the intrinsic scatter in the r_{52}–L_{IR} relation is greater than that in the r_{52}–Σ_{SFR} relation. Note that in the case of equally sloped L'_{CO}–L_{IR} relations for different J (for example, the linear relations found by Liu et al. 2015), a correlation between L_{IR} and excitation would also not be expected.

In Figure 13, we show the flux ratios of CO(4–3) and CO(5–4) over CO(2–1), a proxy of the excitation in the CO ladder, as a function of Σ_{SFR}. As anticipated, our galaxies at $\langle z\rangle = 1.2$ probe the low Σ_{SFR} regime at this redshift, compared to the sources studied in Daddi et al. (2015) and the recent work by Valentino et al. (2020a). Overall, the modest mid-J excitation of the ASPECS sources appears to naturally follow from the fact that we are probing galaxies with, on average, more moderate surface densities of star formation. We also compare to the models from Narayanan & Krumholz (2014), who have computed theoretical CO ladders for unresolved observations of galaxies, parameterized by Σ_{SFR}. While the models qualitatively agree and appear to work reasonably well for r_{52}-ratio transition, they seem to overpredict the r_{42}-ratio for the galaxies in our sample.

7.2. Increasing Excitation with Redshift

The CO(3–2) selected galaxies at $z \geqslant 2$ appear to have intrinsically higher excitation, on average, than the CO(2–1) selected galaxies at $z < 2$. This applies not only to the high-J lines, but also for the excitation in CO(3–2). This observation is robust against the sample being CO flux-selected; because the volume probed in CO(2–1) at $z < 2$ is merely a factor 1.75× smaller, at least some sources with a similarly high r_{31} should have been found at $z < 2$, if they are equally common at both redshifts (such a high r_{31} would be indicated by an as high r_{21}, which is not suggested by the LVG modeling).

The increased excitation at $z \geqslant 2$ compared to $z < 2$ suggests an intrinsic evolution between the ISM conditions in massive main-sequence galaxies at these redshifts. There are several reasons why more excited CO gas may be anticipated in SFGs going out to higher redshift. SFGs at fixed stellar mass are known to decrease in size (as measured in the rest-frame optical; van der Wel et al. 2014), while they increase in average SFR (e.g., Whitaker et al. 2014; Schreiber et al. 2015). This means that the SFR surface density increases with redshift for main-sequence galaxies at fixed mass (e.g., Wuyts et al. 2013), which drives the ambient radiation field. Indeed, there are indications that the dust temperature increases with redshift (e.g., Magdis et al. 2012; Béthermin et al. 2015; Schreiber et al. 2018, but see Dudzevičiūtė et al. 2020), which is linked to the main radiation field intensity. As discussed in Section 7.1, the CO excitation is expected to increase with these quantities, as they can drive the density and temperature in the clouds.[27]

We compare the excitation to a range of properties, finding that the galaxies with greater excitation at higher redshift indeed have both higher L_{IR} and, more importantly, Σ_{SFR}. This behavior is illustrated in Figure 14. To quantify the increase with Σ_{SFR}, we add the LVG model predictions for the r_{52} ratio to Figure 13, now also including galaxies at $z = 2$–3 for which we do not directly measure this line ratio. While there is substantial scatter for the individual models, they broadly support the scenario of increasing excitation with Σ_{SFR}.

The trend in Figure 13 can also be understood more fundamentally as a trend with molecular gas surface density, as a high surface density of gas would also drive the CO excitation upwards.[28] In that context, it is interesting to note that several of the galaxies at $z \approx 2.5$ are found to have a more compact dust distribution, compared to some of the sources at $z \approx 1.5$ (Rujopakarn et al. 2019; Kaasinen et al. 2020).

The difference in excitation between the CO(2−1) and CO(3−2)-selected samples at $z \geqslant 2$ and $z < 2$ raises the question to what extent our r_{21} and r_{31} are representative of the broader population of galaxies at these redshifts. Whereas the higher r_{31} at $z \geqslant 2$ could in principle be the result of the CO-flux selection (see Section 7.4), it appears that at the current sensitivity ASPECS can pick up sources with similar gas

[27] Bolatto et al. (2015) point out that a stronger ambient radiation field only drives the low-J excitation upwards if this emission does not arise in a colder, more extended molecular gas reservoir, but is well mixed with the star formation. This is consistent with our data (see Appendix A), but needs to be verified with higher resolution observations.

[28] From a radiative transfer perspective the line ratio will increase with an increasing CO density per velocity gradient (i.e., N_{H_2}/dv for a constant CO abundance), because this drives the line opacity and increases the line trapping and thereby the excitation. Therefore, unless the high column density (gas surface density) is compensated by a linearly increasing turbulence (dv) one naturally expects an increasing excitation with increasing gas surface density. In addition, it is plausible that higher column densities correlate with higher volume densities which will again drive the excitation upwards.

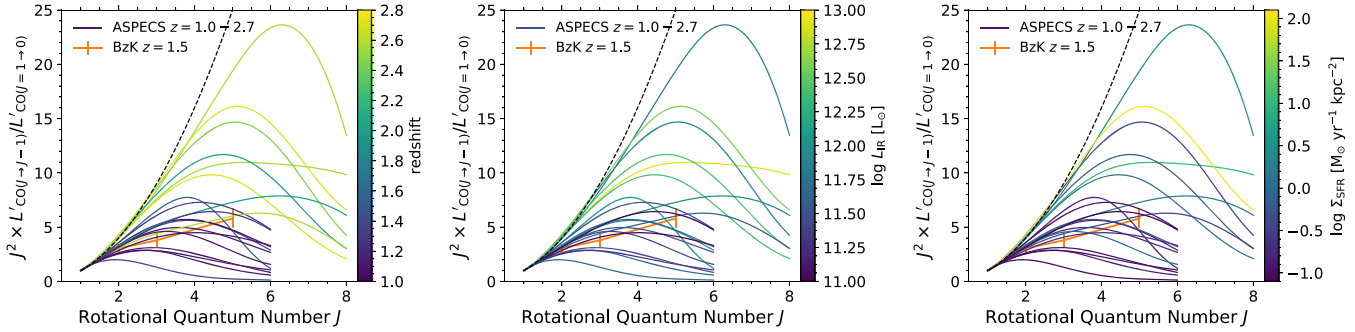

Figure 14. ASPECS CO ladders from the two-component LVG models (see Figure 8) colored by redshift (left), L_{IR} (center) and Σ_{SFR} (right). The ladders are now shown in units of $J^2 \times L'_{CO}$, normalized to $L'_{CO(1-0)}$, for an easy comparison with the figures in units of line flux shown throughout the paper. While the overall excitation increases with redshift, we also observe a range in excitation at fixed redshift. The increase in excitation is correlated with an increase in both L_{IR} and Σ_{SFR}.

masses but with, for example, a factor $\sim 2\times$ lower excitation in r_{31} (see Figure 9 in Boogaard et al. 2019). The conclusions here are limited by the fact we are limited by the low number of massive sources in the volume in the first place (see Figure 5 in Boogaard et al. 2019).[29] At $z < 2$, we probe well below the knee of the CO luminosity function, while at $z \geqslant 2$, we are on or slightly above the knee (Decarli et al. 2019). The same appears true in the context of the IR LF (e.g., Gruppioni et al. 2013). This suggests we are probing the representative part in terms of the cosmic ρ_{H_2}, in particular at $z < 2$. Indeed, the individual detections are the dominant contributors to the total $\rho_{H_2}(z = 2.0 - 3.1)$ (Decarli et al. 2019) and not the corrections for sources that fall below the detection limit.

7.3. The Low-J Excitation

7.3.1. Constraints on r_{21} at z = 1.0–1.6

From our two-component LVG model we find $r_{21} = 0.75 \pm 0.11$ for the CO(2–1) selected galaxies at $z = 1.0$–1.6. This is in good agreement with the average value of $r_{21} = 0.76 \pm 0.09$ for the three massive SFGs at $z = 1.5$ (Daddi et al. 2015, which are well described by a two-component model).

On the other hand, comparing the dust luminosity at rest-frame 850 μm to the CO(1–0) luminosity—which is inferred from the CO(2–1) line using this value of r_{21}, because we do not have direct observations of CO(1–0) at this redshift range—we find that the dust luminosity under-predicts that of the gas. If such a relation holds (Scoville et al. 2016), this may suggest that the average excitation in CO(2–1) is higher (Figure 10). Looking in detail at the galaxies from Daddi et al. (2015), two out of three galaxies have an r_{21} consistent with unity (0.92 ± 0.23 and 1.02 ± 0.20), while the average subthermal excitation is driven by the third source ($r_{21} = 0.48 \pm 0.08$). For comparison, in SMGs at higher redshift, the average r_{21} is often found to be close to, or consistent with unity: $r_{21} = 0.84 \pm 0.13$ (Bothwell et al. 2013) and $r_{21} = 1.11 \pm 0.08$ (Spilker et al. 2014, i.e., suprathermal, though we caution this sample potentially suffers from line-dependent differences in the lensing amplification), though the number of SMGs with direct constraints on r_{21} is still small and significantly spread in redshift (Carilli et al. 2010; Riechers et al. 2013; Aravena et al. 2016). If we would assume that our sources are on average better described by a single-component model we find a higher value of $r_{21} = 0.83 \pm 0.12$. However, given that both the mid-J excitation and L_{IR} are lower than the *BzK* galaxies, this appears less likely. The fact that the single-component model is formally consistent with the two-component solution, as well as thermalized CO, highlights that we are considering relatively small differences in excitation in the first place, compared to the observational uncertainties. In any case, as observations of CO(1–0) around $z \approx 1.2$ are impossible given the atmospheric opacity, detailed characterizations of the multiline CO ladders are key to make progress here.

It should be noted that there are several reasons why the comparison with the dust luminosity as a molecular gas tracer may break down in the first place. If the mass-weighted dust temperature in our sources is higher compared to the sample from Scoville et al. (2016) this would increase the dust luminosity at fixed gas mass, relieving the need for thermalized CO. However, even if the luminosity-weighted dust temperature varies, the mass-weighted dust temperature will not vary so strongly (Scoville et al. 2016). It is also not clear that our galaxies would have a very different dust-opacity slope (β). A discrepancy between the dust and CO emission could also happen if the dust emission is distinct from the CO emission (e.g., in the case of constant gas-to-dust ratio, but a strong dust temperature gradient, or opacity effects). It is not clear that our galaxies would be very distinct from the calibration sample in this respect. However, we are probing a fainter regime in L_ν(850 μm), where the calibration sample is mostly local, while the sources at comparable redshifts are generally higher luminosity. Furthermore, our data at 1.2 mm and 3.0 mm probes further down the Rayleigh–Jeans tail than some of the earlier observations. The Scoville relation also breaks for galaxies with a strongly sub-solar metallicity and for that reason Scoville et al. (2016) restrict their sample to galaxies with $M_* \geqslant 2 \times 10^{10}\ M_\odot$. However, the ASPECS galaxies are generally more massive than this and have (super-)solar metallicities (Boogaard et al. 2019). Finally, we do not exclude the possibility that the apparent discrepancy (on average) is driven by low number statistics, as the majority of the sample is consistent within the intrinsic scatter in the relation.

[29] Note that while we would, in principle, pick up sources with larger gas masses but lower excitation, this would require ASPECS to probe a larger volume at similar depth. Initial efforts are made in this direction through WIDE ASPECS (R. Decarli et al. 2020, in preparation), a survey that covers approximately seven times the area of the ASPECS-LP, albeit at a depth that is more shallow.

7.3.2. Measurement of r_{31} at z = 2.0–2.7

Stacking the CO(3–2)-selected galaxies at $\langle z \rangle = 2.5$, we directly derive an $r_{31} = 0.77 \pm 0.14$, which is supported by the average value from the LVG modeling of all individual sources at $z = 2.0$–2.7 ($r_{31} = 0.80 \pm 0.14$). This value is significantly higher than found in the lower redshift *BzK*-selected SFGs at $z = 1.5$ (Daddi et al. 2015; $r_{31} = 0.42 \pm 0.15$; ranging from 0.27–0.57), which has implications for the measurement of the cosmic molecular gas density (we will come back to this in Section 7.5). Studying two massive main-sequence galaxies at $z = 2.3$, Bolatto et al. (2015) found higher ratios consistent with thermalized CO: $r_{31} = 0.92 \pm 0.11$ and $r_{31} = 1.17 \pm 0.17$ (plus two lower limits of $\geqslant$0.57 and $\geqslant$0.79). The SMGs at $z = 2$ show a wide range of excitation values, as discussed in Riechers et al. (2020). Early studies found a relatively low average ($r_{31} = 0.52 \pm 0.09$ Ivison et al. 2011; Bothwell et al. 2013), while more recently, Sharon et al. (2016) found an average of $r_{31} = 0.78 \pm 0.27$. At higher redshift, Spilker et al. (2014) reports $r_{31} = 0.87 \pm 0.06$, although these lensed sources are arguably more extreme. Overall, the different samples at $z = 2$–3 show a significant spread in their r_{31} ratio (see also Riechers et al. 2020), driven by different selection methods picking up galaxies with different ambient conditions in their ISM. In that context, ASPECS provides a well-defined sample for further investigation —flux-limited in CO(3–2) and followed up in CO(1–0)—which probes fainter $L_{\rm IR}$ than the typical samples of SMGs. A contribution from the AGN is not expected to dominate the low-*J* lines and we do not find a clear correlation between r_{31} and the presence of an X-ray AGN.

7.3.3. Consistency with the Model Results

The fairly high excitation in the low-*J* lines is generally consistent with the densities of $\geqslant 10^4$ cm^{-3} found in the (constant density) PDR modeling of the low-*J* CO and [C I] lines (though we caution that the different types of models should not be blindly compared, given the differences in underlying assumptions). From a radiative transfer perspective, it is rather easy to excite CO(2–1), even at modest densities and temperatures, and slightly less so for CO(3–2). Note the effective floor on the gas temperature at each redshift is set by the Cosmic Microwave Background, which measures $T_{\rm CMB} = 6$ K at $z = 1.2$ and 10 K at $z = 2.5$. For comparison, the temperatures corresponding to the energy level differences for the (dominant) $\Delta J = 1$ collisional excitations are $T_{1\rightarrow 2} = (E_2 - E_1)/k_B = 11.1$ K and $T_{2\rightarrow 3} = 16.6$ K, respectively, where k_B is the Boltzmann constant. As such, unless galaxies harbor extended low-excitation reservoirs (addressed in Appendix A), the levels of low-*J* excitation found in this work are not unexpected.

7.4. Broader Implications of the Flux-limited Survey

Because ASPECS is a flux-limited survey, without any target preselection, it also provides additional information on the CO excitation in the whole population of gas mass-selected galaxies, beyond just the detected sources. The observed CO luminosity at different redshifts depends on the product of $r_{J1} M_{\rm mol}\ \alpha_{\rm CO}{}^{-1}$ (Equation (4)) and hence three selection effects are at play. At a given redshift we would first detect the sources with the highest gas mass (at fixed $\alpha_{\rm CO}$) and the highest luminosity at a given gas mass, i.e., the sources with the highest excitation in their low-*J* lines. Given that we detect approximately half of the massive main-sequence galaxies at $z = 1$–3 (Boogaard et al. 2019), this implies that the galaxies that we did not detect will have a less massive gas reservoir (and/or higher $\alpha_{\rm CO}$) and/or lower CO excitation in the $J = 2$ and $J = 3$ levels. For that reason, in particular for galaxies toward the lower stellar mass and SFR end of the ASPECS sample at a given redshift (i.e., the faint end of the survey), where we are less complete, the average excitation of the low-*J* levels may be lower. By the same argument, the fact that we do not detect any galaxies in the mid-/high-*J* CO lines alone that are in principle detectable in the low-*J* CO(2–1) or CO(3–2) lines, implies that the excitation in their mid-/high-*J* levels will not be significantly above the detected samples at the respective redshifts, for galaxies with comparable gas masses (at fixed $\alpha_{\rm CO}$).

7.5. Implications for the Cosmic Molecular Gas Density

By measuring the CO luminosity in galaxies without any preselection over a well-defined cosmic volume, ASPECS is conducting the deepest census of the cosmic molecular gas density, $\rho_{\rm H_2}(z)$, to date (Decarli et al. 2016a, 2019, 2020). This relies on the excitation corrections from the $J \geqslant 2$ lines back to CO(1–0). In the initial results from ASPECS, these have been assumed to follow a single CO ladder, as measured for *BzK*-selected SFGs by Daddi et al. (2015) at $\langle z \rangle = 1.5$, up to CO(4–3),[30] as these were considered to be the closest analogs of the sources observed with ASPECS at the time.[31] With our study of the CO excitation in the ASPECS galaxies—the actual sources that defined $\rho_{\rm H_2}(z)$—we can now revisit these assumptions in more detail.

Our result that the average excitation increases between $z < 2$ and $z \geqslant 2$ has important implications for $\rho_{\rm H_2}(z)$. Our results support the earlier assumptions for the excitation corrections at $z < 2$. Adopting the new CO ladders (Table 3) does not significantly alter the constraints on $\rho_{\rm H_2}$ at $z < 2$, with the largest change being a 25% decrease at $z = 0.7$–1.2 (based on r_{41}). In contrast, the significantly higher excitation at $z \geqslant 2$ implies a factor 2× decrease in $\rho_{\rm H_2}$ compared to earlier results, for CO(3–2) at $z = 2.0$–3.1 (see also Riechers et al. 2020) and CO(4–3) at $z = 3.0$–4.5. It should be noted that we currently do lack direct constraints on the excitation for CO(4–3)-selected samples at $z = 3.0$–4.5. However, based on the results from this paper, we do not expect the average excitation for the sources contributing to the measurement of $\rho_{\rm H_2}$ to be lower than at $z = 2.5$ (and certainly not as low as in Daddi et al. 2015). Note that this decrease is in line with the models underpredicting the earlier measurements of $\rho_{\rm H_2}(z > 2)$ (e.g., Popping et al. 2019).

In summary, we make new recommendations for the average CO ladders to be used for the measurement of the cosmic molecular gas density (the two-component models from Table 3). The constraints on $\rho_{\rm H_2}(z)$ using the new excitation corrections are presented and discussed in Decarli et al. (2020). Our results, combined with those of Riechers et al. (2020), show that direct measurement of the CO(1–0) transition (where accessible) as well as constructing more complete CO ladders, in order to characterize the CO excitation and physical

[30] Daddi et al. (2015) did not measure the excitation in CO(4–3), but interpolating their CO ladder yields $r_{41} = 0.31 \pm 0.06$ (see Decarli et al. 2016b).

[31] The full range of results was considered to be bracketed between two extreme cases: MW-like low-excitation conditions and thermalized CO, see Appendix B in Decarli et al. (2019).

conditions in the cold ISM, are essential to make progress in further constraining the cosmic molecular gas density.

8. Summary and Conclusions

This paper presents a study of the carbon monoxide (CO) excitation, atomic carbon ([C I]) emission, and ISM conditions in a sample of 22 SFGs at $z = 0.46$–3.60. These galaxies have been observed as part of the ASPECS-LP, designed to provide a cosmic inventory of molecular gas by selecting galaxies purely by their CO and dust-continuum emission in ALMA Bands 3 and 6, without any preselection. These galaxies are known to lie on, above, and below the main sequence of SFGs at their respective redshifts (Aravena et al. 2019, 2020; Boogaard et al. 2019). We detect a total of 34 CO $J \rightarrow J-1$ lines with $J = 1$ up to 8 (+21 upper limits, up to $J = 10$) and 6 [C I] $^3P_1 \rightarrow {}^3P_0$ and $^3P_2 \rightarrow {}^3P_1$ lines (+12 upper limits). This includes follow-up observations of seven sources at $z = 1.99$–2.70 in CO(1–0) from VLASPECS (Riechers et al. 2020), that we analyze here in concert with the ASPECS data.

The ASPECS galaxies have lower infrared luminosities ($L_{\rm IR}$) and SFR surface densities ($\Sigma_{\rm SFR}$) than earlier, targeted samples of SFGs and submillimeter galaxies (including lensed samples) at similar redshifts (Bothwell et al. 2013; Spilker et al. 2014; Daddi et al. 2015). We study the CO excitation of the CO(2–1) and CO(3–2) selected samples and compare them to the average CO ladders of the targeted samples. We focus on two redshift bins, $\langle z\rangle = 1.2$ and $\langle z\rangle = 2.5$, at which we cover both a low/mid-J CO transition and a mid/high-J CO transition with ASPECS.

We find that half of the galaxies at $\langle z\rangle = 1.2$ show remarkably similar excitation, up to CO(5–4), similar to that observed in a sample of four *BzK*-color-selected SFGs at $\langle z\rangle = 1.5$ (Daddi et al. 2015), while the remaining sources are consistent with lower excitation. The range in excitation suggests that a warm and/or dense component, indicated by the higher excitation, is not omnipresent in galaxies at these redshifts. We detect the high-$J \geqslant 6$ lines in several galaxies at $\langle z\rangle = 2.5$, indicating that the high-J excitation is comparable to the levels in local starbursts and slightly lower than SMGs at similar redshifts (Bothwell et al. 2013), although half of the sources selected by their CO(3–2) emission are not detected in their high-J lines.

Stacking all the CO and [C I] transitions that we cover with ASPECS (including non-detections), we find our galaxies at $\langle z\rangle = 1.2$ show, on average, lower excitation than *BzK*-selected galaxies. This is consistent with a picture in which the CO excitation is driven by the SFR surface density $\Sigma_{\rm SFR}$, broadly matching model predictions (although the models do not fully reproduce our observations). For the galaxies at $\langle z\rangle = 2.5$, the stacking reveals an average $r_{31} = 0.77 \pm 0.14$ and $r_{71} = 0.19 \pm 0.04$, broadly comparable to SMGs at this epoch, as well as local starburst galaxies

We present the average excitation corrections for cold gas mass-selected galaxies at $z = 1.0$–1.6 and $z = 2.0$–2.7, based on the interpolation of the CO ladders using (single- and) two-component LVG models. These models predict $r_{21} = 0.75 \pm 0.11$ at $z < 2$, similar to the *BzK*-selected SFGs (Daddi et al. 2015).

We place our sources on the empirical correlations between $L'_{\rm CO(1-0)}$ and dust luminosity at rest-frame 850 μm, probing significantly lower $L_\nu(850\,\mu{\rm m})$ than the earlier samples at $z > 0$, and find good agreement for the CO(3–2)-selected sources. However, we find that the dust luminosity on average overpredicts the CO(1–0) luminosity for the CO(2–1)-selected sample. This either implies that the average r_{21} at $\langle z\rangle = 1.2$ is higher, or that the assumptions going into the correlation break down for these sources.

Comparing our [C I](1–0) and [C I](2–1) observations to the literature, we find that the $L_{\rm [C\,I]}/L_{\rm IR}$ ratio of our sample is similar to main-sequence galaxies, as observed by Valentino et al. (2018). We find an average neutral atomic carbon abundance of $[{\rm C\,I}]/[{\rm H_2}] = (1.9 \pm 0.4) \times 10^{-5}$. This is comparable to the abundance measured in the main-sequence galaxies and the MW, but lower than what is measured in SMGs (although this apparent discrepancy is degenerate with the assumption of a different $\alpha_{\rm CO}$; Valentino et al. 2018). Modeling the CO, [C I], and $L_{\rm IR}$ emission using the PDRTOOLBOX indicates densities $\geqslant 10^4$ cm^{-3}, generally consistent with the (fairly high) excitation in the low-J lines.

The interpolated CO ladders suggest that the intrinsic excitation is higher for the sources at $z \geqslant 2$ compared to $z < 2$, even in the lower-J lines such as CO(3–2). The excitation difference is robust against the ASPECS selection function and correlated with $L_{\rm IR}$ and $\Sigma_{\rm SFR}$. This implies an intrinsic evolution in the ISM conditions of massive SFGs between these redshifts, which we link to an increase in the surface density of star formation (and gas) in SFGs with redshift.

Because ASPECS is a flux-limited survey, it also provides additional information on the CO excitation in the whole population of gas mass-selected galaxies. Being most sensitive to galaxies with the highest excitation at a given gas mass (at fixed $\alpha_{\rm CO}$), this suggests that the average excitation in sources with comparable gas masses (at fixed $\alpha_{\rm CO}$) may be lower toward the faint end of the survey. At the same time, the non-detection of galaxies in their mid-/high-J alone (which are in principle detectable in their low-J lines), implies that the average excitation is not much higher.

The galaxies studied in this paper are the same as those constraining the CO luminosity function and the cosmic molecular gas density, $\rho_{\rm H_2}$, as measured by ASPECS. The increased excitation in the CO-selected galaxies at $z \geqslant 2$ compared to those at $z < 2$ implies a decrease in the inferred $\rho_{\rm H_2}(z \geqslant 2)$ compared to earlier measurements (Decarli et al. 2016a, 2019). We make recommendations for the average CO excitation in CO-flux-limited samples of galaxies, to be adopted in the constraints on $\rho_{\rm H_2}(z)$ from the complete ASPECS survey, presented in Decarli et al. (2020).

The observations presented here have extended the sample of SFGs at $z = 1$–3 with constraints on their CO excitation and atomic carbon emission. As these are the same galaxies through which the CO luminosity function is measured, characterizing them in detail is key to further our constraints on the cosmic molecular gas density. Further study of such well-defined (flux-limited) samples with multiline observations will be instrumental to gain a complete picture of the ISM conditions in SFGs across cosmic time.

We would like to thank the anonymous referee for an insightful and constructive report. The author is also grateful to Francesco Valentino for providing early access to the data from Valentino et al. (2020a), that appeared on the arXiv while this paper was under review. This paper makes use of the following ALMA data: ADS/JAO.ALMA#2016.1.00324.L. ALMA is a

partnership of ESO (representing its member states), NSF (USA) and NINS (Japan), together with NRC (Canada), NSC and ASIAA (Taiwan), and KASI (Republic of Korea), in cooperation with the Republic of Chile. The Joint ALMA Observatory is operated by ESO, AUI/NRAO, and NAOJ. The National Radio Astronomy Observatory is a facility of the National Science Foundation operated under cooperative agreement by Associated Universities, Inc. F.W. acknowledges support from ERC grant 740246 (Cosmic_Gas). Este trabajo contó con el apoyo de CONICYT + PCI + INSTITUTO MAX PLANCK DE ASTRONOMIA MPG190030. D.R. acknowledges support from the National Science Foundation under grant Nos. AST-1614213 and AST-1910107. D.R. also acknowledges support from the Alexander von Humboldt Foundation through a Humboldt Research Fellowship for Experienced Researchers. I.R.S. acknowledges support from STFC (ST/T000244/1). M.K. acknowledges support from the International Max Planck Research School for Astronomy and Cosmic Physics at Heidelberg University (IMPRS-HD). T.D.-S. acknowledges support from the CASSACA and CONICYT fund CAS-CONICYT Call 2018. H.I. acknowledges support from JSPS KAKENHI grant No. JP19K23462.

Facilities: ALMA, VLA, VLT:Yepun (MUSE).

Software: TOPCAT (Taylor 2005), GNUASTRO (Akhlaghi & Ichikawa 2015), IPYTHON (Perez & Granger 2007), NUMPY (van der Walt et al. 2011), MATPLOTLIB (Hunter 2007), ASTROPY (The Astropy Collaboration et al. 2013; Price-Whelan et al. 2018).

Appendix A
Similar Widths for the Low-*J* and High-*J* CO Lines

Previous studies have suggested that some SMGs at $z = 2$–4 have line widths in CO(1–0) that are larger than in the higher-*J* transitions (e.g., Ivison et al. 2011; although the difference is rather subtle, about ∼15%, which is within the limits of our data). Together with the observation that the excitation models to the high-*J* CO lines underpredicted the total molecular gas mass in these sources (by a factor of ∼1.5–4.5; Riechers et al. 2011b), this suggested the presence of extended low-excitation gas reservoirs in some SMGs, but, notably, not in all cases (e.g., Riechers et al. 2011a; Hodge et al. 2012). If there would be extended emission in CO(1–0), this complicates estimates of total molecular gas mass from the higher-*J* lines.

We find that the line widths of the different CO and [C I] lines are consistent (see Figure 2), including the CO(1–0) lines. There is one outlier, 3mm.12, which has a potential low-S/N broad component that should be confirmed by future observations (Riechers et al. 2020; this line has S/N < 3 in the fit where the line widths are tied together). The strong CO luminosity relative to the dust emission (see Section 5.4), even when assuming thermalized CO, suggests that we are not missing a large volume of molecular gas in CO(2–1) and CO(3–2) that would be probed by the dust. Furthermore, from an excitation perspective it is very unlikely to have gas that radiates purely in CO(1–0) and not at all in CO(2–1), which is only attainable at very low $n_{\rm H_2}$ and $T_{\rm kin}$. Looking at other SFGs at the same redshift, in the *BzK*-selected galaxies at $z = 1.5$ (Daddi et al. 2015) the line widths are also found to be very similar between CO(2–1) (Daddi et al. 2010) and CO(1–0) (Aravena et al. 2014; although the errors on the latter are significant). Similarly, Bolatto et al. (2015) found consistent line widths and spatial extent between CO(3–2) and CO(1–0) in two massive main-sequence galaxies at $z = 2.3$. In summary, while we cannot conclusively rule out their presence with the current observations, we do not see clear evidence of a large volumes of cold molecular gas that are not traced by the relatively low-*J* CO lines. This supports the use of these transitions in inferring the molecular gas mass.

Appendix B
Spectral Line Fits

Gaussian fits to the spectral lines of CO and [C I], performed as detailed in Section 3.1, are shown in Figure 15. The best-fit parameters are reported in Table 6. For each source, we fit a single redshift and line width for all lines simultaneously.

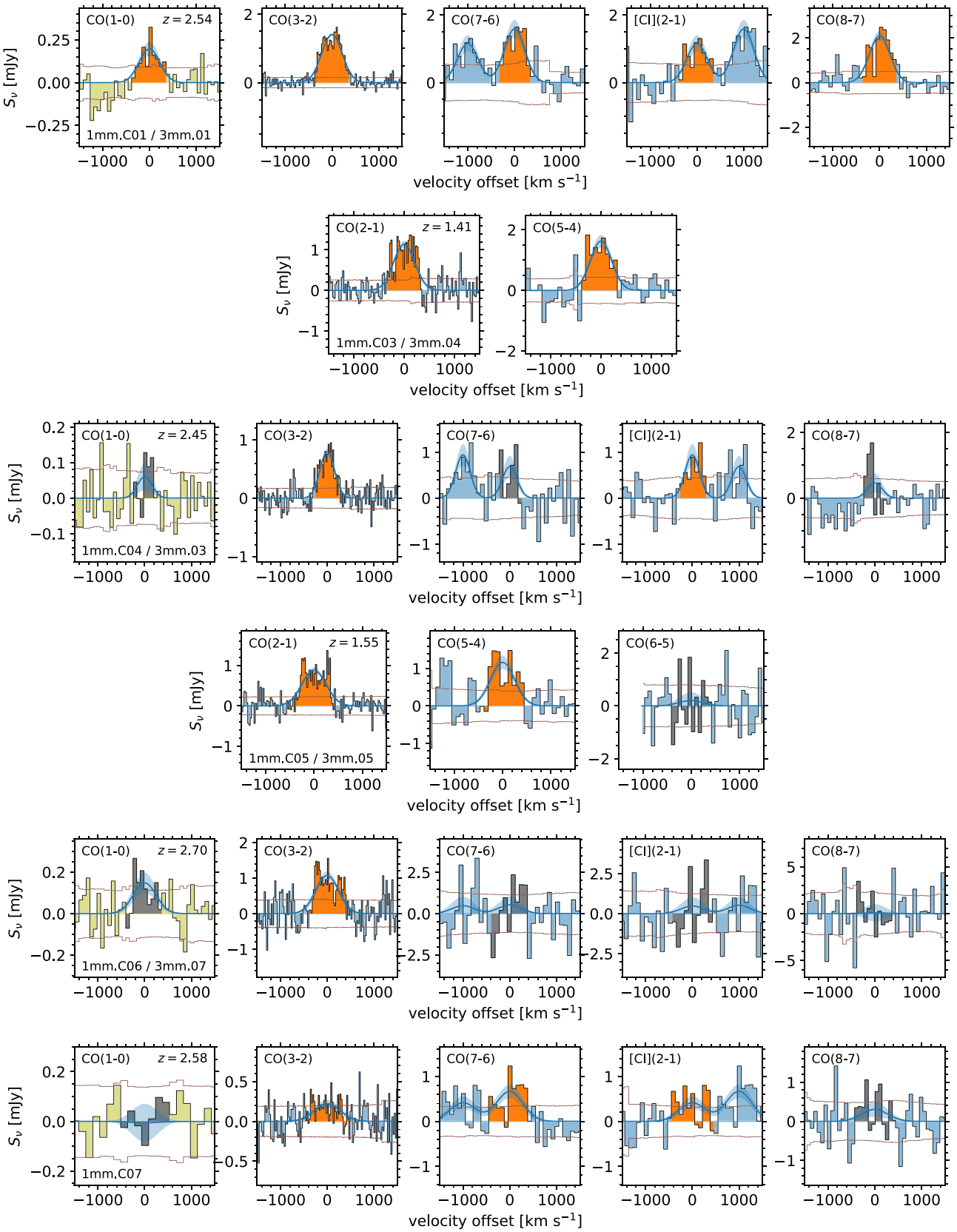

Figure 15. Gaussian fits to the ^{12}CO and [C I] lines in the ASPECS galaxies. The groups of panels (max 2 per row) show the different transitions (indicated top left) in a single galaxy (identified in the bottom left of the leftmost panel). The spectra are shown in blue (ASPECS) and yellow (VLA) and are binned in the *Ka* band and Band 6 for visualization purposes (except for 3mm.08 and 3mm.11 with very narrow lines). The brown line shows the $\pm 1\sigma$ rms noise. The best fit for all lines (tied together in redshift and line width) and a 1σ confidence interval are shown by the blue line and shading. The channels indicated in orange (gray) fall within 1.4 × FWHM (i.e., 90% of the flux) for a detection (non-detection).

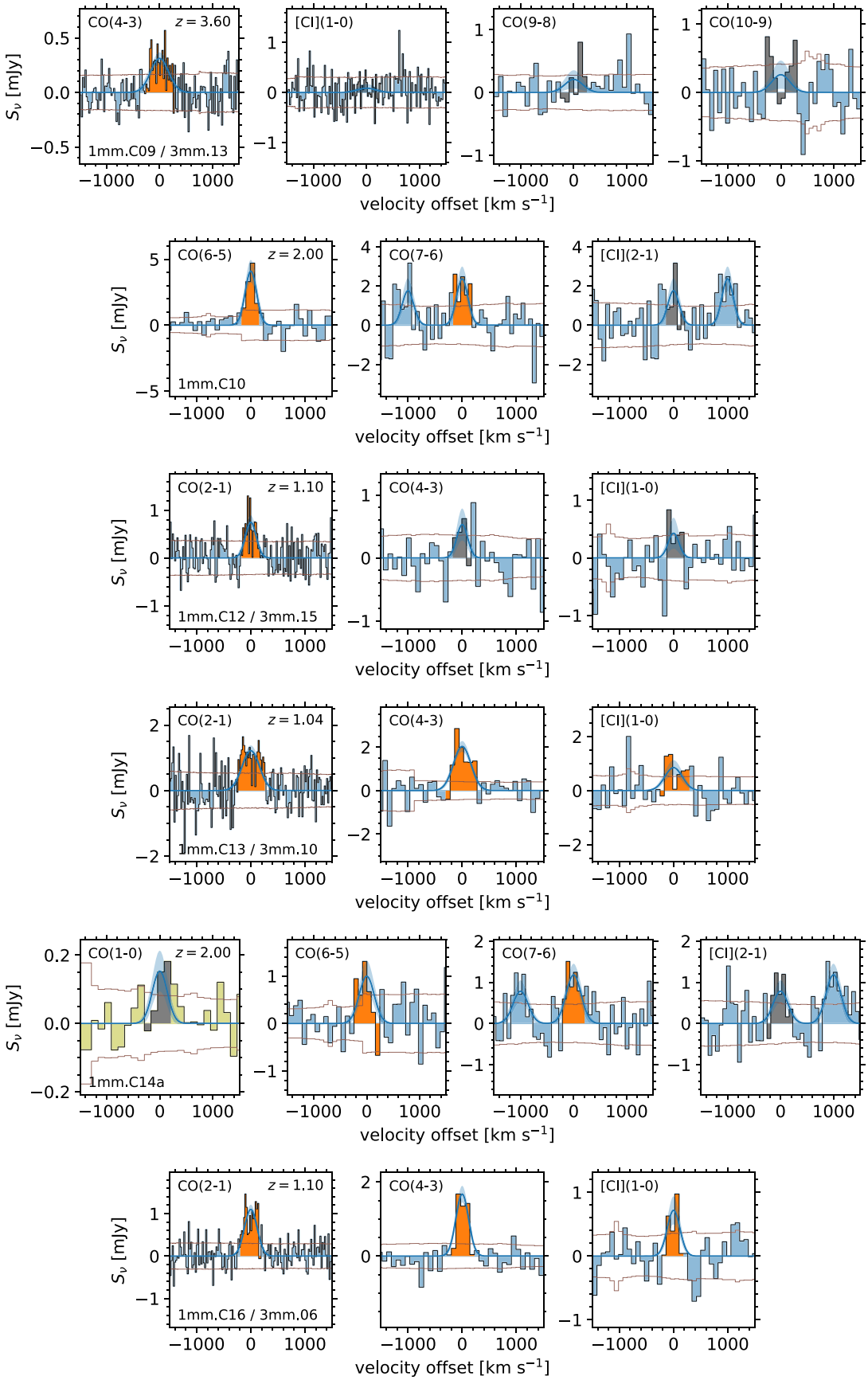

Figure 15. (Continued.)

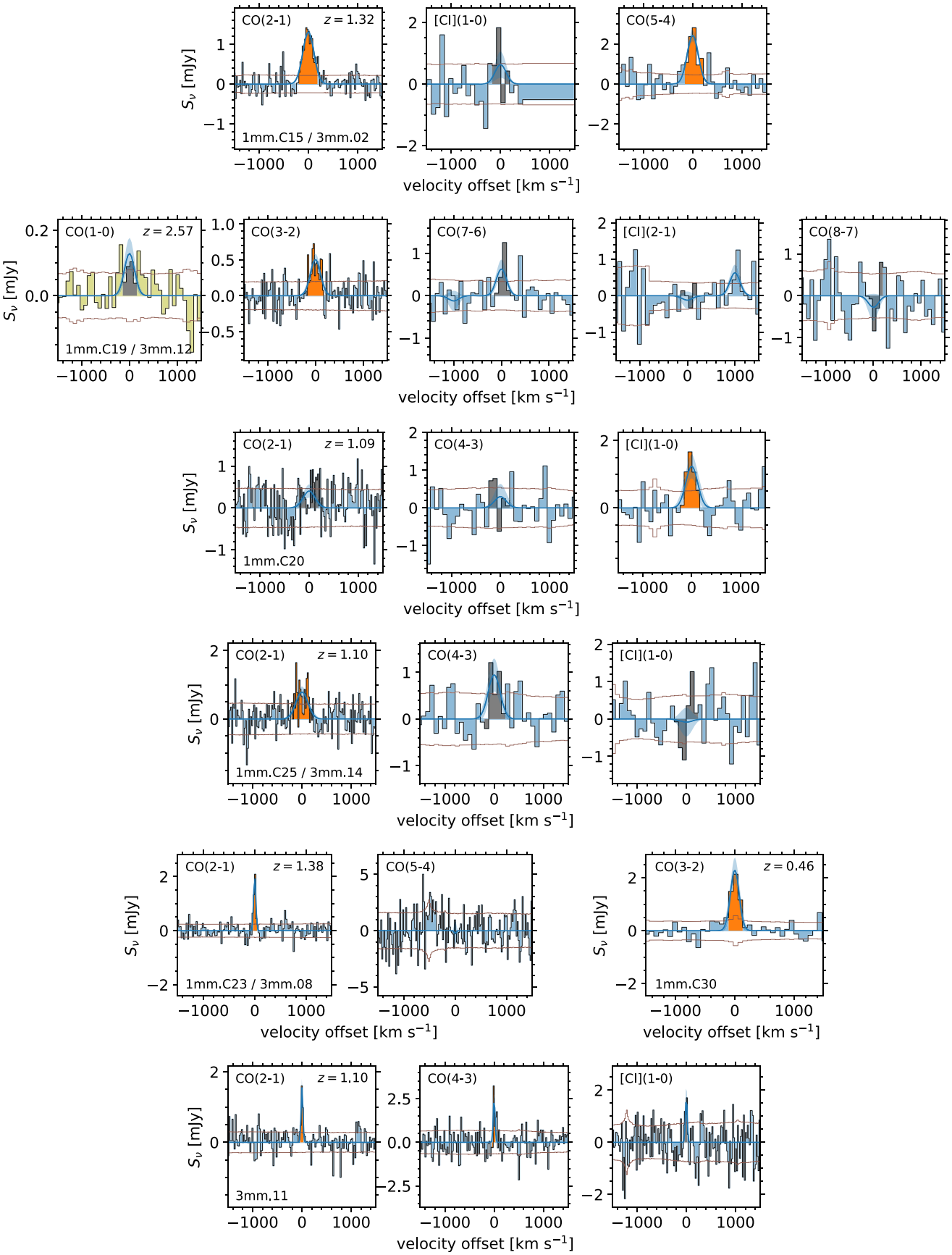

Figure 15. (Continued.)

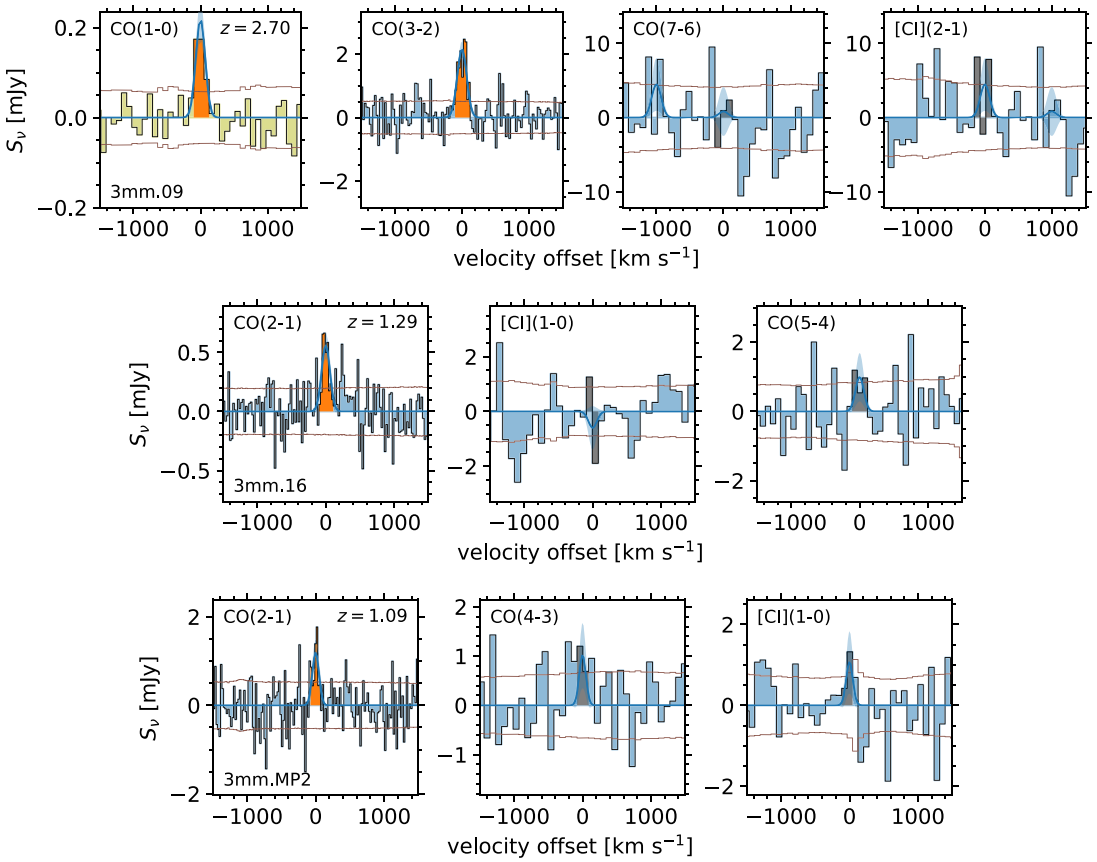

Figure 15. (Continued.)

Table 6
Spectral Line Properties Determined with Gaussian Fits

ID 1mm	ID 3mm	z	FWHM (km s^{-1})	Line	Frequency (GHz)	S^V (Jy km s^{-1})	L' ($\times 10^9$ K km s^{-1} pc^2)	r_{J1}	r_{J2}
(1)	(2)	(3)	(4)	(5)	(6)	(7)	(8)	(9)	(10)
1mm.C01	3mm.01	2.5437 ± 0.0001	518 ± 18	CO(3–2)	97.582 ± 0.002	0.78 ± 0.02	25.9 ± 0.8	0.79 ± 0.17	⋯
				CO(7–6)	227.633 ± 0.006	0.88 ± 0.15	5.4 ± 0.9	0.16 ± 0.04	⋯
				[C I](2–1)	228.392 ± 0.006	0.64 ± 0.13	3.9 ± 0.8	⋯	⋯
				CO(8–7)	260.127 ± 0.007	1.16 ± 0.12	5.4 ± 0.5	0.17 ± 0.04	⋯
				CO(1–0)	32.529 ± 0.001	0.11 ± 0.02	32.7 ± 6.8	⋯	⋯
1mm.C03	3mm.04	1.4142 ± 0.0001	498 ± 39	CO(2–1)	95.491 ± 0.005	0.60 ± 0.04	15.8 ± 1.2	⋯	⋯
				CO(5–4)	238.697 ± 0.013	0.86 ± 0.11	3.6 ± 0.5	⋯	0.23 ± 0.03
1mm.C04	3mm.03	2.4535 ± 0.0002	367 ± 31	CO(3–2)	100.130 ± 0.004	0.31 ± 0.02	9.7 ± 0.7	1.46 ± 0.91	⋯
				CO(7–6)	233.577 ± 0.010	0.27 ± 0.09	1.6 ± 0.5	0.23 ± 0.16	⋯
				[C I](2–1)	234.356 ± 0.010	0.37 ± 0.09	2.1 ± 0.5	⋯	⋯
				CO(8–7)	266.920 ± 0.012	0.18 ± 0.12	0.8 ± 0.5	0.12 ± 0.11	⋯
				CO(1–0)	33.378 ± 0.002	0.02 ± 0.01	6.7 ± 4.2	⋯	⋯
1mm.C05	3mm.05	1.5503 ± 0.0002	587 ± 48	CO(2–1)	90.397 ± 0.006	0.55 ± 0.04	17.2 ± 1.3	⋯	⋯
				CO(5–4)	225.962 ± 0.015	0.73 ± 0.11	3.6 ± 0.6	⋯	0.21 ± 0.04
				CO(6–5)	271.135 ± 0.018	0.13 ± 0.20	0.4 ± 0.7	⋯	⋯
1mm.C06	3mm.07	2.6956 ± 0.0004	572 ± 68	CO(3–2)	93.570 ± 0.009	0.65 ± 0.07	24.1 ± 2.6	0.81 ± 0.28	⋯
				CO(7–6)	218.273 ± 0.021	0.32 ± 0.31	2.2 ± 2.1	0.07 ± 0.07	⋯
				[C I](2–1)	219.001 ± 0.021	0.29 ± 0.34	2.0 ± 2.3	⋯	⋯
				CO(8–7)	249.431 ± 0.024	0.06 ± 0.57	0.3 ± 2.9	0.01 ± 0.10	⋯
				CO(1–0)	31.191 ± 0.003	0.09 ± 0.03	29.9 ± 10.1	⋯	⋯
1mm.C07	⋯	2.5805 ± 0.0006	658 ± 109	CO(3–2)	96.577 ± 0.017	0.16 ± 0.03	5.3 ± 1.1	−4.19 ± 54.58	⋯
				CO(7–6)	225.288 ± 0.040	0.47 ± 0.10	2.9 ± 0.6	−2.31 ± 30.13	⋯
				[C I](2–1)	226.040 ± 0.040	0.29 ± 0.10	1.8 ± 0.6	⋯	⋯
				CO(8–7)	257.448 ± 0.046	0.22 ± 0.13	1.0 ± 0.6	−0.82 ± 10.63	⋯
				CO(1–0)	32.194 ± 0.006	−0.00 ± 0.05	−1.3 ± 16.5	⋯	⋯
1mm.C09	3mm.13	3.6008 ± 0.0005	397 ± 80	CO(4–3)	100.208 ± 0.011	0.13 ± 0.02	4.4 ± 0.8	⋯	
				[C I](1–0)	106.972 ± 0.012	0.04 ± 0.04	1.1 ± 1.0	⋯	⋯
				CO(9–8)	225.375 ± 0.026	0.09 ± 0.06	0.6 ± 0.4	⋯	⋯
				CO(10–9)	250.386 ± 0.028	0.11 ± 0.09	0.6 ± 0.5	⋯	⋯
1mm.C10	⋯	1.9975 ± 0.0002	248 ± 44	CO(6–5)	230.682 ± 0.015	1.09 ± 0.22	5.9 ± 1.2	⋯	⋯
				CO(7–6)	269.106 ± 0.018	0.63 ± 0.17	2.5 ± 0.7	⋯	⋯
				[C I](2–1)	270.004 ± 0.018	0.47 ± 0.17	1.9 ± 0.7	⋯	⋯
1mm.C12	3mm.15	1.0963 ± 0.0001	235 ± 50	CO(2–1)	109.975 ± 0.008	0.19 ± 0.04	3.0 ± 0.6	⋯	⋯
				CO(4–3)	219.934 ± 0.016	0.13 ± 0.06	0.5 ± 0.3	⋯	0.18 ± 0.09
				[C I](1–0)	234.779 ± 0.016	0.11 ± 0.07	0.4 ± 0.2	⋯	⋯
1mm.C13	3mm.10	1.0364 ± 0.0001	380 ± 42	CO(2–1)	113.207 ± 0.007	0.49 ± 0.06	7.1 ± 0.9	⋯	⋯
				CO(4–3)	226.396 ± 0.013	0.82 ± 0.10	3.0 ± 0.4	⋯	0.42 ± 0.07
				[C I](1–0)	241.678 ± 0.014	0.35 ± 0.11	1.1 ± 0.4	⋯	⋯
1mm.C14a	⋯	1.9966 ± 0.0003	332 ± 64	CO(6–5)	230.755 ± 0.021	0.35 ± 0.11	1.9 ± 0.6	0.18 ± 0.09	⋯
				CO(7–6)	269.191 ± 0.025	0.42 ± 0.10	1.7 ± 0.4	0.16 ± 0.07	⋯
				[C I](2–1)	270.089 ± 0.025	0.28 ± 0.09	1.1 ± 0.4	⋯	⋯
				CO(1–0)	38.468 ± 0.004	0.05 ± 0.02	10.7 ± 4.2	⋯	⋯
1mm.C16	3mm.06	1.0952 ± 0.0001	275 ± 27	CO(2–1)	110.029 ± 0.004	0.32 ± 0.03	5.2 ± 0.5	⋯	⋯
				CO(4–3)	220.042 ± 0.008	0.49 ± 0.07	2.0 ± 0.3	⋯	0.38 ± 0.06
				[C I](1–0)	234.894 ± 0.009	0.21 ± 0.06	0.7 ± 0.2	⋯	⋯
1mm.C15	3mm.02	1.3167 ± 0.0001	266 ± 19	CO(2–1)	99.512 ± 0.003	0.37 ± 0.03	8.4 ± 0.6	⋯	⋯

Table 6
(Continued)

ID 1mm	ID 3mm	z	FWHM (km s^{-1})	Line	Frequency (GHz)	S^V (Jy km s^{-1})	L' ($\times 10^9$ K km s^{-1} pc^2)	r_{J1}	r_{J2}
(1)	(2)	(3)	(4)	(5)	(6)	(7)	(8)	(9)	(10)
				[C I](1–0)	212.442 ± 0.006	0.18 ± 0.12	0.9 ± 0.6	⋯	⋯
				CO(5–4)	248.747 ± 0.007	0.69 ± 0.08	2.5 ± 0.3	⋯	0.30 ± 0.04
1mm.C19	3mm.12	2.5739 ± 0.0002	254 ± 43	CO(3–2)	96.756 ± 0.006	0.14 ± 0.02	4.6 ± 0.8	0.43 ± 0.18	⋯
				CO(7–6)	225.707 ± 0.014	0.17 ± 0.06	1.1 ± 0.4	0.10 ± 0.05	⋯
				[C I](2–1)	226.460 ± 0.014	−0.03 ± 0.06	−0.2 ± 0.4	⋯	⋯
				CO(8–7)	257.926 ± 0.016	−0.07 ± 0.09	−0.4 ± 0.4	−0.03 ± 0.04	⋯
				CO(1–0)	32.254 ± 0.002	0.04 ± 0.01	10.7 ± 4.0	⋯	⋯
1mm.C20	⋯	1.0931 ± 0.0002	287 ± 83	CO(2–1)	110.140 ± 0.013	0.12 ± 0.05	2.0 ± 0.8	⋯	⋯
				CO(4–3)	220.264 ± 0.026	0.09 ± 0.10	0.4 ± 0.4	⋯	0.19 ± 0.22
				[C I](1–0)	235.131 ± 0.028	0.38 ± 0.11	1.3 ± 0.4	⋯	⋯
1mm.C25	3mm.14	1.0982 ± 0.0002	289 ± 65	CO(2–1)	109.874 ± 0.010	0.24 ± 0.05	3.9 ± 0.8	⋯	⋯
				CO(4–3)	219.732 ± 0.020	0.29 ± 0.11	1.2 ± 0.4	⋯	0.30 ± 0.13
				[C I](1–0)	234.564 ± 0.021	−0.03 ± 0.12	−0.1 ± 0.4	⋯	⋯
1mm.C23	3mm.08	1.3821 ± 0.0000	50 ± 7	CO(2–1)	96.778 ± 0.001	0.11 ± 0.01	2.7 ± 0.3	⋯	⋯
				CO(5–4)	241.912 ± 0.002	−0.01 ± 0.06	−0.0 ± 0.2	⋯	−0.02 ± 0.09
1mm.C30	⋯	0.4580 ± 0.0001	176 ± 36	CO(3–2)	237.170 ± 0.012	0.43 ± 0.08	0.5 ± 0.1	⋯	⋯
⋯	3mm.11	1.0964 ± 0.0000	44 ± 7	CO(2–1)	109.970 ± 0.001	0.07 ± 0.01	1.2 ± 0.2	⋯	⋯
				CO(4–3)	219.924 ± 0.002	0.12 ± 0.03	0.5 ± 0.1	⋯	0.40 ± 0.11
				[C I](1–0)	234.769 ± 0.002	0.08 ± 0.03	0.3 ± 0.1	⋯	⋯
⋯	3mm.09	2.6976 ± 0.0001	165 ± 22	CO(3–2)	93.520 ± 0.003	0.38 ± 0.05	13.9 ± 1.7	1.09 ± 0.27	⋯
				CO(7–6)	218.158 ± 0.007	0.14 ± 0.58	1.0 ± 3.9	0.08 ± 0.31	⋯
				[C I](2–1)	218.885 ± 0.007	0.78 ± 0.63	5.3 ± 4.2	⋯	⋯
				CO(1–0)	31.175 ± 0.001	0.04 ± 0.01	12.8 ± 2.7	⋯	⋯
Faint.1mm.C20	3mm.16	1.2938 ± 0.0001	144 ± 32	CO(2–1)	100.504 ± 0.005	0.09 ± 0.02	1.9 ± 0.4	⋯	⋯
				[C I](1–0)	214.559 ± 0.010	−0.09 ± 0.12	−0.4 ± 0.6	⋯	⋯
				CO(5–4)	251.225 ± 0.012	0.15 ± 0.11	0.5 ± 0.4	⋯	0.28 ± 0.21
⋯	MP.3mm.2	1.0873 ± 0.0001	115 ± 33	CO(2–1)	110.448 ± 0.005	0.15 ± 0.04	2.3 ± 0.6	⋯	⋯
				CO(4–3)	220.878 ± 0.010	0.12 ± 0.08	0.5 ± 0.3	⋯	0.21 ± 0.15
				[C I](1–0)	235.788 ± 0.011	0.13 ± 0.10	0.5 ± 0.3	⋯	⋯

Note. (1) ASPECS-LP 1mm ID. (2) ASPECS-LP 3mm ID. (3) Redshift. (4) Line full-width at half-maximum (FWHM). (5) Line identification. (6) Observed line frequency. (7) Integrated line flux, $S^V = \int S_\nu dv$ (sometimes called $S\Delta v$). (8) Line luminosity (Equation (2)). (9) Line luminosity ratio with CO(1–0) (Equation (3)). (10) Line luminosity ratio with CO(2–1).

ORCID iDs

Leindert A. Boogaard https://orcid.org/0000-0002-3952-8588
Paul van der Werf https://orcid.org/0000-0001-5434-5942
Axel Weiss https://orcid.org/0000-0003-4678-3939
Gergö Popping https://orcid.org/0000-0003-1151-4659
Roberto Decarli https://orcid.org/0000-0002-2662-8803
Fabian Walter https://orcid.org/0000-0003-4793-7880
Manuel Aravena https://orcid.org/0000-0002-6290-3198
Rychard Bouwens https://orcid.org/0000-0002-4989-2471
Dominik Riechers https://orcid.org/0000-0001-9585-1462
Jorge González-López https://orcid.org/0000-0003-3926-1411
Ian Smail https://orcid.org/0000-0003-3037-257X
Chris Carilli https://orcid.org/0000-0001-6647-3861
Melanie Kaasinen https://orcid.org/0000-0002-1173-2579
Emanuele Daddi https://orcid.org/0000-0002-3331-9590
Pierre Cox https://orcid.org/0000-0003-2027-8221
Tanio Díaz-Santos https://orcid.org/0000-0003-0699-6083
Hanae Inami https://orcid.org/0000-0003-4268-0393
Paulo C. Cortes https://orcid.org/0000-0002-3583-780X

References

Akhlaghi, M., & Ichikawa, T. 2015, ApJS, 220, 1
Alaghband-Zadeh, S., Chapman, S. C., Swinbank, A. M., et al. 2013, MNRAS, 435, 1493
Andreani, P., Retana-Montenegro, E., Zhang, Z. Y., et al. 2018, A&A, 615, A142
Aravena, M., Boogaard, L., Gónzalez-López, J., et al. 2020, ApJ, 901, 79
Aravena, M., Carilli, C., Daddi, E., et al. 2010, ApJ, 718, 177
Aravena, M., Decarli, R., Gónzalez-López, J., et al. 2019, ApJ, 882, 136
Aravena, M., Hodge, J. A., Wagg, J., et al. 2014, MNRAS, 442, 558
Aravena, M., Spilker, J. S., Bethermin, M., et al. 2016, MNRAS, 457, 4406
Béthermin, M., Daddi, E., Magdis, G., et al. 2015, A&A, 573, A113
Bisbas, T. G., Papadopoulos, P. P., & Viti, S. 2015, ApJ, 803, 37
Bisbas, T. G., van Dishoeck, E. F., Papadopoulos, P. P., et al. 2017, ApJ, 839, 90
Blain, A. W., Smail, I., Ivison, R. J., Kneib, J. P., & Frayer, D. T. 2002, PhR, 369, 111
Bolatto, A. D., Leroy, A. K., Rosolowsky, E., Walter, F., & Blitz, L. 2008, ApJ, 686, 948
Bolatto, A. D., Warren, S. R., Leroy, A. K., et al. 2015, ApJ, 809, 175
Bolatto, A. D., Wolfire, M., & Leroy, A. K. 2013, ARA&A, 51, 207
Boogaard, L. A., Brinchmann, J., Bouché, N., et al. 2018, A&A, 619, A27
Boogaard, L. A., Decarli, R., González-López, J., et al. 2019, ApJ, 882, 140
Bothwell, M. S., Aguirre, J. E., Aravena, M., et al. 2017, MNRAS, 466, 2825
Bothwell, M. S., Smail, I., Chapman, S. C., et al. 2013, MNRAS, 429, 3047
Bourne, N., Dunlop, J. S., Simpson, J. M., et al. 2019, MNRAS, 482, 3135
Brisbin, D., Aravena, M., Daddi, E., et al. 2019, A&A, 628, A104
Cañameras, R., Yang, C., Nesvadba, N. P. H., et al. 2018, A&A, 620, A61
Carilli, C. L., Daddi, E., Riechers, D., et al. 2010, ApJ, 714, 1407
Carilli, C. L., & Walter, F. 2013, ARA&A, 51, 105
Chabrier, G. 2003, PASP, 115, 763
Da Cunha, E., Charlot, S., & Elbaz, D. 2008, MNRAS, 388, 1595
Da Cunha, E., Walter, F., Smail, I. R., et al. 2015, ApJ, 806, 110
Daddi, E., Bournaud, F., Walter, F., et al. 2010, ApJ, 713, 686
Daddi, E., Cimatti, A., Renzini, A., et al. 2004, ApJ, 617, 746
Daddi, E., Dannerbauer, H., Liu, D., et al. 2015, A&A, 577, A46
Dannerbauer, H., Daddi, E., Riechers, D. A., et al. 2009, ApJ, 698, 178
Dannerbauer, H., Harrington, K., Díaz-Sánchez, A., et al. 2019, AJ, 158, 34
Decarli, R., Aravena, M., & Boogaard, L. 2020, ApJ, 902, 110
Decarli, R., Walter, F., Aravena, M., et al. 2016a, ApJ, 833, 69
Decarli, R., Walter, F., Aravena, M., et al. 2016b, ApJ, 833, 70
Decarli, R., Walter, F., Gónzalez-López, J., et al. 2019, ApJ, 882, 138
Dickman, R. L., Snell, R. L., & Schloerb, F. P. 1986, ApJ, 309, 326
Dudzevičiūtė, U., Smail, I., Swinbank, A. M., et al. 2020, MNRAS, 494, 3828
Dunlop, J. S., McLure, R. J., Biggs, A. D., et al. 2017, MNRAS, 466, 861
Elbaz, D., Dickinson, M., Hwang, H. S., et al. 2011, A&A, 533, A119
Fixsen, D. J., Bennett, C. L., & Mather, J. C. 1999, ApJ, 526, 207
Frerking, M. A., Keene, J., Blake, G. A., & Phillips, T. G. 1989, ApJ, 344, 311
Genzel, R., Tacconi, L. J., Gracia-Carpio, J., et al. 2010, MNRAS, 407, 2091
Genzel, R., Tacconi, L. J., Lutz, D., et al. 2015, ApJ, 800, 20
Gerin, M., & Phillips, T. G. 2000, ApJ, 537, 644
Glover, S. C., Clark, P. C., Micic, M., & Molina, F. 2015, MNRAS, 448, 1607
González-López, J., Decarli, R., Pavesi, R., et al. 2019, ApJ, 882, 139
González-López, J., Novak, M., Decarli, R., et al. 2020, ApJ, 897, 91
Greve, T. R., Leonidaki, I., Xilouris, E. M., et al. 2014, ApJ, 794, 142
Gruppioni, C., Pozzi, F., Rodighiero, G., et al. 2013, MNRAS, 432, 23
Habing, H. 1968, BAN, 19, 421
Harrington, K. C., Yun, M. S., Magnelli, B., et al. 2018, MNRAS, 474, 3866
Hildebrand, R. 1983, QJRAS, 24, 267
Hodge, J. A., Carilli, C. L., Walter, F., et al. 2012, ApJ, 760, 11
Hunter, J. D. 2007, CSE, 9, 90
Ikeda, M., Oka, T., Tatematsu, K., Sekimoto, Y., & Yamamoto, S. 2002, ApJS, 139, 467
Illingworth, G. D., Magee, D., Oesch, P. A., et al. 2013, ApJS, 209, 6
Israel, F. P., Rosenberg, M. J. F., & van der Werf, P. 2015, A&A, 578, A95
Ivison, R. J., Papadopoulos, P. P., Smail, I., et al. 2011, MNRAS, 412, 1913
Jiao, Q., Zhao, Y., Lu, N., et al. 2019, ApJ, 880, 133
Jin, S., Daddi, E., Magdis, G. E., et al. 2019, ApJ, 887, 144
Kaasinen, M., Scoville, N., Walter, F., et al. 2019, ApJ, 880, 15
Kaasinen, M., Walter, F., Novak, M., et al. 2020, ApJ, 899, 37
Kamenetzky, J., Rangwala, N., & Glenn, J. 2017, MNRAS, 471, 2917
Kamenetzky, J., Rangwala, N., Glenn, J., Maloney, P. R., & Conley, A. 2014, ApJ, 795, 174
Kaufman, M. J., Wolfire, M. G., & Hollenbach, D. J. 2006, ApJ, 644, 283
Kennicutt, R. C., & Evans, N. J. 2012, ARA&A, 50, 531
Kirkpatrick, A., Sharon, C., Keller, E., & Pope, A. 2019, ApJ, 879, 41
Koekemoer, A. M., Ellis, R. S., McLure, R. J., et al. 2013, ApJS, 209, 3
Liang, L., Feldmann, R., Faucher-Giguère, C.-A., et al. 2018, MNRAS Lett., 478, L83
Liu, D., Gao, Y., Isaak, K., et al. 2015, ApJL, 810, L14
Lu, N., Zhao, Y., Díaz-Santos, T., et al. 2017, ApJS, 230, 1
Luo, B., Brandt, W. N., Xue, Y. Q., et al. 2017, ApJS, 228, 2
Magdis, G. E., Daddi, E., Béthermin, M., et al. 2012, ApJ, 760, 6
Magnelli, B., Boogaard, L., Decarli, R., et al. 2020, ApJ, 892, 66
McKee, C. F., & Ostriker, E. C. 2007, ARA&A, 45, 565
McMullin, J., Waters, B., Schiebel, D., Young, W., & Golap, K. 2007, in ASP Conf. Ser. 376, CASA Architecture and Applications, ed. R. Shaw, F. Hill, & D. Bell (San Francisco, CA: ASP), 127
Meijerink, R., Spaans, M., & Israel, F. P. 2007, A&A, 461, 793
Narayanan, D., & Krumholz, M. R. 2014, MNRAS, 442, 1411
Nesvadba, N. P., Cañameras, R., Kneissl, R., et al. 2019, A&A, 624, A23
Newville, M., Otten, R., Nelson, A., et al. 2019, lmfit/lmfit-py v0.9.13, Zenodo, doi:10.5281/zenodo.2620617
Noeske, K. G., Weiner, B. J., Faber, S. M., et al. 2007, ApJL, 660, L43
Obreschkow, D., Heywood, I., Klöckner, H.-R., & Rawlings, S. 2009, ApJ, 702, 1321
Ojha, R., Stark, A. A., Hsieh, H. H., et al. 2001, ApJ, 548, 253
Papadopoulos, P. P., Thi, W. F., & Viti, S. 2004, MNRAS, 351, 147
Perez, F., & Granger, B. E. 2007, CSE, 9, 21
Pham, D. T., & Castellani, M. 2009, Proc. Inst. Mech. Eng. Part C: J. Mech. Eng. Sci., 223, 2919
Planck Collaboration, Ade, P. A. R., Aghanim, N., et al. 2016, A&A, 594, A13
Popping, G., Decarli, R., Man, A. W. S., et al. 2017, A&A, 602, A11
Popping, G., Pillepich, A., Somerville, R. S., et al. 2019, ApJ, 882, 137
Pound, M. W., & Wolfire, M. G. 2008, in ASP Conf. Ser. 394, Astronomical Data Analysis Software and Systems, ed. R. W. Argyle, P. S. Bunclark, & J. R. Lewis (San Francisco, CA: ASP), 654
Price-Whelan, A. M., Sipőcz, B. M., Günther, H. M., et al. 2018, AJ, 156, 123
Privon, G. C., Narayanan, D., & Davé, R. 2018, ApJ, 867, 102
Rangwala, N., Maloney, P. R., Glenn, J., et al. 2011, ApJ, 743, 94
Riechers, D. A., Boogaard, L. A., Decarli, R., et al. 2020, ApJL, 896, L21
Riechers, D. A., Bradford, C. M., Clements, D. L., et al. 2013, Natur, 496, 329
Riechers, D. A., Carilli, C. L., Maddalena, R. J., et al. 2011a, ApJL, 739, L32
Riechers, D. A., Carilli, C. L., Walter, F., & Momjian, E. 2010, ApJL, 724, L153
Riechers, D. A., Hodge, J., Walter, F., Carilli, C. L., & Bertoldi, F. 2011b, ApJL, 739, L31
Riechers, D. A., Pavesi, R., Sharon, C. E., et al. 2019, ApJ, 872, 7
Rosenberg, M. J., van der Werf, P. P., Aalto, S., et al. 2015, ApJ, 801, 72
Rosenberg, M. J. F., Kazandjian, M. V., van der Werf, P. P., et al. 2014, A&A, 564, A126
Rujopakarn, W., Daddi, E., Rieke, G. H., et al. 2019, ApJ, 882, 107
Sanders, D. B., & Mirabel, I. F. 1996, ARA&A, 34, 749
Sargent, M. T., Daddi, E., Béthermin, M., et al. 2014, ApJ, 793, 19

Schneider, N., Simon, R., Kramer, C., et al. 2003, A&A, 406, 915
Schreiber, C., Elbaz, D., Pannella, M., et al. 2018, A&A, 609, A30
Schreiber, C., Pannella, M., Elbaz, D., et al. 2015, A&A, 575, A74
Scoville, N., Aussel, H., Sheth, K., et al. 2014, ApJ, 783, 84
Scoville, N., Sheth, K., Aussel, H., et al. 2016, ApJ, 820, 83
Sharon, C. E., Riechers, D. A., Hodge, J., et al. 2016, ApJ, 827, 1
Skelton, R. E., Whitaker, K. E., Momcheva, I. G., et al. 2014, ApJS, 214, 24
Solomon, P., & Vanden Bout, P. 2005, ARA&A, 43, 677
Solomon, P. M., Downes, D., & Radford, S. J. E. 1992, ApJL, 398, L29
Solomon, P. M., Rivolo, A. R., Barrett, J., & Yahil, A. 1987, ApJ, 319, 730
Spilker, J. S., Marrone, D. P., Aguirre, J. E., et al. 2014, ApJ, 785, 149
Stutzki, J., Graf, U. U., Haas, S., et al. 1997, ApJL, 477, L33
Tacconi, L. J., Genzel, R., Neri, R., et al. 2010, Natur, 463, 781
Tacconi, L. J., Genzel, R., Saintonge, A., et al. 2018, ApJ, 853, 179
Tacconi, L. J., Neri, R., Genzel, R., et al. 2013, ApJ, 768, 74
Talia, M., Pozzi, F., Vallini, L., et al. 2018, MNRAS, 476, 3956
Taylor, M. B. 2005, in ASP Conf. Ser. 347, Astronomical Data Analysis Software and Systems XIV, ed. P. Shopbell, M. Britton, & R. Ebert (San Francisco, CA: ASP), 29
The Astropy Collaboration, Robitaille, T. P., Tollerud, E. J., et al. 2013, A&A, 558, A33
Tielens, A. G. G. M., & Hollenbach, D. 1985a, ApJ, 291, 747
Tielens, A. G. G. M., & Hollenbach, D. 1985b, ApJ, 291, 722
Valentino, F., Daddi, E., Puglisi, A., et al. 2020a, A&A, 641, A155
Valentino, F., Magdis, G. E., Daddi, E., et al. 2018, ApJ, 869, 27
Valentino, F., Magdis, G. E., Daddi, E., et al. 2020b, ApJ, 890, 24
Vallini, L., Tielens, A. G. G. M., Pallottini, A., et al. 2019, MNRAS, 490, 4502
van der Walt, S., Colbert, S. C., & Varoquaux, G. 2011, CSE, 13, 22
van der Wel, A., Bell, E. F., Häussler, B., et al. 2012, ApJS, 203, 24
van der Wel, A., Franx, M., van Dokkum, P. G., et al. 2014, ApJ, 788, 28
van der Werf, P. P., Isaak, K. G., Meijerink, R., et al. 2010, A&A, 518, L42
Walter, F., Decarli, R., Aravena, M., et al. 2016, ApJ, 833, 67
Walter, F., Weiß, A., Downes, D., Decarli, R., & Henkel, C. 2011, ApJ, 730, 18
Weiß, A., De Breuck, C., Marrone, D. P., et al. 2013, ApJ, 767, 88
Weiß, A., Downes, D., Henkel, C., & Walter, F. 2005, A&A, 429, L25
Weiß, A., Downes, D., Neri, R., et al. 2007, Astro, 467, 955
Weiß, A., Henkel, C., Downes, D., & Walter, F. 2003, A&A, 409, L41
Weiss, A., Downes, D., Walter, F., & Henkel, C. 2007, in ASP Conf. Ser. 375, From Z-Machines to ALMA: (Sub)Millimeter Spectroscopy of Galaxies, ed. A. J. Baker et al. (San Francisco, CA: ASP), 25
Whitaker, K. E., Franx, M., Leja, J., et al. 2014, ApJ, 795, 104
Wuyts, S., Förster Schreiber, N. M., Nelson, E. J., et al. 2013, ApJ, 779, 135
Yang, C., Omont, A., Beelen, A., et al. 2017, A&A, 608, A144